

Fall 2010

Experimental investigation of key assumptions in analytical failure criteria for sheet metal forming

Tugce Kasikci

University of New Hampshire, Durham

Follow this and additional works at: <https://scholars.unh.edu/thesis>

Recommended Citation

Kasikci, Tugce, "Experimental investigation of key assumptions in analytical failure criteria for sheet metal forming" (2010). *Master's Theses and Capstones*. 583.

<https://scholars.unh.edu/thesis/583>

This Thesis is brought to you for free and open access by the Student Scholarship at University of New Hampshire Scholars' Repository. It has been accepted for inclusion in Master's Theses and Capstones by an authorized administrator of University of New Hampshire Scholars' Repository. For more information, please contact nicole.hentz@unh.edu.

EXPERIMENTAL INVESTIGATION OF KEY ASSUMPTIONS IN
ANALYTICAL FAILURE CRITERIA FOR SHEET METAL
FORMING

BY

TUGCE KASIKCI

Baccalaureate of Science, Middle East Technical University, 2008

THESIS

Submitted to the University of New Hampshire

in Partial Fulfilment of

the Requirements for the Degree of

Master of Science

in

Mechanical Engineering

September, 2010

UMI Number: 1486997

All rights reserved

INFORMATION TO ALL USERS

The quality of this reproduction is dependent upon the quality of the copy submitted.

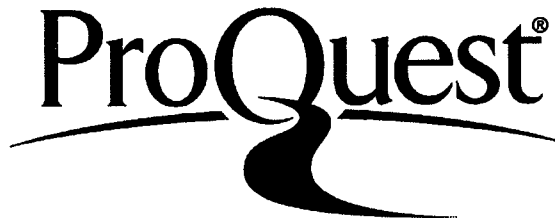
In the unlikely event that the author did not send a complete manuscript and there are missing pages, these will be noted. Also, if material had to be removed, a note will indicate the deletion.



UMI 1486997

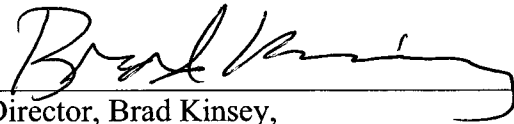
Copyright 2010 by ProQuest LLC.

All rights reserved. This edition of the work is protected against unauthorized copying under Title 17, United States Code.

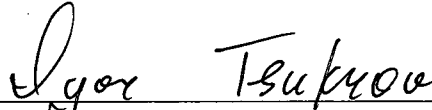


ProQuest LLC
789 East Eisenhower Parkway
P.O. Box 1346
Ann Arbor, MI 48106-1346

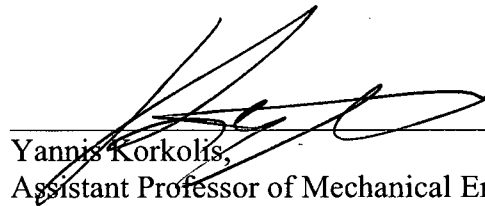
This thesis has been examined and approved.



Thesis Director, Brad Kinsey,
Associate Professor of Mechanical Engineering



Igor Tsukrov,
Professor of Mechanical Engineering



Yannis Korkolis,
Assistant Professor of Mechanical Engineering

7-16-10

Date

ACKNOWLEDGEMENTS

Support from NSF (CMMI-0654124) for my research is gratefully acknowledged.

TABLE OF CONTENTS

ACKNOWLEDGEMENTS	iii
LIST OF TABLES	vi
LIST OF FIGURES	vii
ABSTRACT	x

CHAPTERS	PAGE
1. INTRODUCTION AND BACKGROUND	1
2. EXPERIMENTAL SET UP.....	9
2.1 Tooling and Specimen Geometries.....	9
2.2. Material Tested.....	14
2.3 Forming Press.....	15
2.4 Digital Imaging Correlation System.....	17
2.4.1 Preparation of the Specimen	18
2.4.2 Post Processing of Digital Images.....	19
3. EXPERIMENTAL RESULTS	27
3.1 Results for M-K Model Key Assumption	33
3.2 Results for Derov et al. Model Key Assumption	41
3.3. Discussions.....	48
4. CONCLUSIONS	53
5. FUTURE WORK.....	55
LIST OF REFERENCES.....	56

APPENDICES	58
APPENDIX A.....	59
APPENDIX B.....	62

LIST OF TABLES

Table 2-1: Dimensions of the various specimen geometries	14
Table 2-2: Material parameters for 1018 Steel used in Marciniak test [10].	15

LIST OF FIGURES

Figure 1-1: Strain-based Forming Limit Diagram with safe, marginal and fail regions labelled [2].	2
Figure 1-2: Schematic of axisymmetric Marciniak test tooling.....	3
Figure 1-3: Strain-based Forming Limit Curves for various uniaxial (U), plane (P) and balanced biaxial (E) prestrains both longitudinal (L) and transverse (T) to the major strain direction for Al 2008-T4 [2]	4
Figure 1-4: Fourteen strain-based FLCs from Graf and Hosford converge to one curve in stress space when analytically converted using Barlat’s 1989 yield criterion [6].	5
Figure 1-5: Schematic of safe (a) and defect (b) regions with varying thicknesses for the Marciniak and Kuczynski model [3].....	6
Figure 1-6: Schematic of the safe (A) and defect (B) regions for the Derov et al. model.....	7
Figure 2-1: Representation of main groups of geometries for the Raghavan modification to Marciniak test.....	10
Figure 2-2: Schematic of various specimen (left) and washer (right) geometries for a) Type i1, b) Type i2, c) Type ii1, d) Type ii2, e) Type ii3, f) Type iii1, g) Type iii2 and h) Type iv specimens.	13
Figure 2-3: Tensile test data for 1018 Steel and power law curve fit for the 0 degree data.....	15
Figure 2-4: Experimental setup.....	17
Figure 2-5: Speckle pattern on loaded specimen.	19
Figure 2-6: Contour plot for locating X- and Y- axis on the specimen	20

Figure 2-7: An example of a grid of extracted nodes on the specimen.	22
Figure 2-8: Pictures of a) physical and b) DIC system measurements for comparison	26
Figure 3-1: Strain paths varying from uniaxial to balanced biaxial cases for the various specimen types.	28
Figure 3-2: Initial strain path ($\Delta\epsilon_2/\Delta\epsilon_1$) versus forming depth at failure.	29
Figure 3-3: Contour plots of major strain with defect orientations shown for a) Type i1, b) Type i2, c) Type ii1, d) Type ii2, e) Type ii3, f) Type iii1, g) Type iii2 and h) Type iv specimens.	32
Figure 3-4: Strain-based Forming Limit Diagram for Steel 1018 from the experimental data for Type i1, ii2, ii3 and iv specimens.	32
Figure 3-5: Strain path curves for the defect node and locations at 2, 5 and 10 mm away in the X-direction for a) Type i1, b) Type i2, c) Type ii1, d) Type ii2, e) Type ii3, f) Type iii1, g) Type iii2 and h) Type iv specimens.	37
Figure 3-6: Major true strain for Type i1 specimen for defect node and node 5 mm away versus normalized time to failure.	37
Figure 3-7: Incremental strain ratios versus forming depth for a) Type i1, b) Type i2, c) Type ii1, d) Type ii2, e) Type ii3, f) Type iii1, g) Type iii2, and h) Type iv specimens.	40
Figure 3-8: Initial strain path versus incremental strain ratio for image directly before failure.	41
Figure 3-9: Critical stress concentration factor (i.e., F-parameter) versus the X-direction location for a) Type i1, b) Type i2, c) Type ii1, d) Type ii2, e) Type ii3, f) Type iii1, g) Type iii2 and h) Type iv specimens.	44

Figure 3-10: Surface plot of critical stress concentration factor (i.e., F-parameter) versus location from defect node for a) Type i2, b) Type ii1 and c) Type iv specimens.46

Figure 3-11: Critical stress concentration factor (i.e., F-parameter) versus distance from the defect node in the X-direction for different specimen types. (F-parameter for Type ii3 is centered to see the effect)47

Figure 3-12: Critical stress concentration factor (i.e., F-parameter) versus initial strain path. (Note that curves represent data 5 and 10 mm away from the defect locations.)48

Figure 3-13: Contour plot of major strain for balanced biaxial case (specimen Type iv).51

Figure B-1: Incremental path showing how to calculate the stress-based FLC. Once one set of failure points is found, the σ_{2A} is incremented and another set is calculated.65

ABSTRACT

EXPERIMENTAL INVESTIGATION OF KEY ASSUMPTIONS IN ANALYTICAL FAILURE CRITERIA FOR SHEET METAL FORMING

by

Tugce Kasikci

University of New Hampshire September 2010

Tearing concerns in sheet metal forming can be predicted based on the strain and stress in the material using analytical models, e.g., the Marciniak Kuczynski (M-K) model and the Derov et al. model respectively. An assumption to these models is that a thin area of concentrated deformation exists which is referred to as the defect region. Other key assumptions for the models are related to when the material is predicted to fail. For the M-K model, the failure is related to the incremental strain ratio inside and outside the defect region. Similarly, for the Derov et al. model, the failure is related to a critical stress concentration factor, i.e., the ratio of the effective stress inside and outside the defect region. In order to investigate these key assumptions, Marciniak tests with coupled Digital Imaging Correlation (DIC) to measure the strain in the material as well as the size of the defect region were conducted on 1018 steel with eight specimen geometries, which varied the strain path from uniaxial to balanced biaxial. The results show that the parameters investigated to predict failure (i.e., the incremental strain ratio and critical stress concentration factor) were not constant for the various strain paths for both analytical models considered.

CHAPTER 1

INTRODUCTION AND BACKGROUND

Sheet metal forming is a vital manufacturing process for the automotive, aerospace, beverage can and other industries. Accurate failure predictions in sheet metal forming can shorten production lead times; reduce the operating and tooling costs; and allow for more aggressive designs. Often during sheet metal forming, it is desirable for the material to undergo significant stretching to achieve a work hardened state which improves the strength of the final product. However, extensive stretching beyond the plastic instability limit of the material will lead to a tearing failure. There is an obvious trade off between inducing a sufficient work hardened state and avoiding tearing failure during tooling and product design.

Tearing failure in sheet metal forming is traditionally predicted to occur when the in-plane strain is above the strain-based Forming Limit Diagram (FLD) (see Fig. 1-1 with “Fail”, “Marginal” and “Safe” regions labelled.). Strain-based FLDs are used because strain can be measured on the surface of the material during and after a deformation process. Keeler [1] was the first to develop strain-based Forming Limit Curves (FLCs) by conducting a series of dome height experiments with specimens of varying widths which created different strain paths to failure.

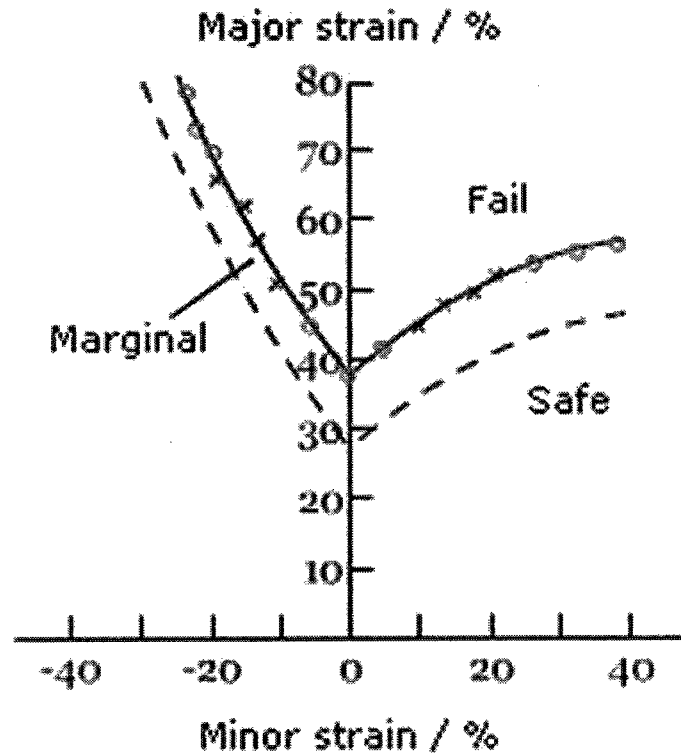


Figure 1-1: Strain-based Forming Limit Diagram with safe, marginal and fail regions labelled [2].

The standard axisymmetric tests to experimentally determine strain-based FLCs are Nakajima tests (with a rigid hemispherical punch) and Marciniak tests (see Fig. 1-2 for a schematic of the Marciniak tooling geometry). With the Marciniak test, the bending and frictional effects are eliminated in the central, test region of interest; therefore, the failure is dependent solely on material effects rather than process effects. At the failure location, major and minor strains are obtained and plotted on a strain-based FLC for each of the different geometries (i.e., strain paths). Details regarding specimen geometries for Marciniak tests will be presented in Chapter 2.

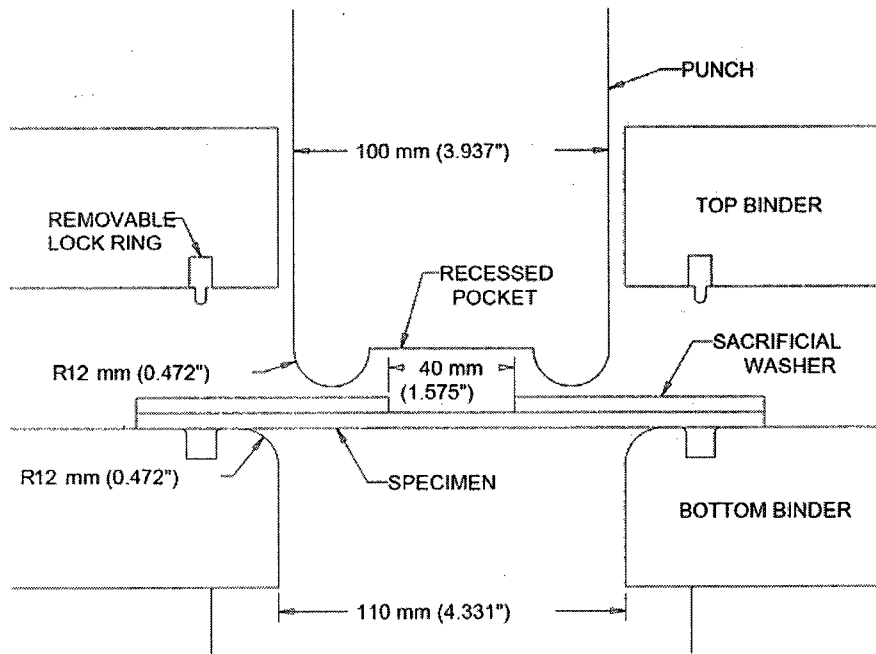


Figure 1-2: Schematic of axisymmetric Marciniak test tooling.

Prestraining the material produces significant changes in strain paths and causes the strain-based FLCs to shift and distort in strain space. Thus, strain-based FLCs are path dependent, which is a major disadvantage in predicting the failure with this criterion. See Fig. 2 from Graf and Hosford [3] showing the strain-based FLCs for Al 2008-T4 with various prestrain values. There is a theoretical predictability to the shifting and distortion of the strain-based FLCs; however, this requires assumptions regarding material parameters (e.g., strength coefficient (K), strain hardening exponent (n), anisotropic parameter (R), etc.) and yield criterion (e.g., Hill's 1948 criterion, Von-Misses criterion, etc.) [4].

While Graf and Hosford results are for prestraining the material through cold rolling, strain paths can vary significantly during forming operations of complex parts causing difficulties in predicting tearing concerns. Thus in numerical simulations, the strain

path of each element would need to be considered to determine failure using a strain-based FLD [5].

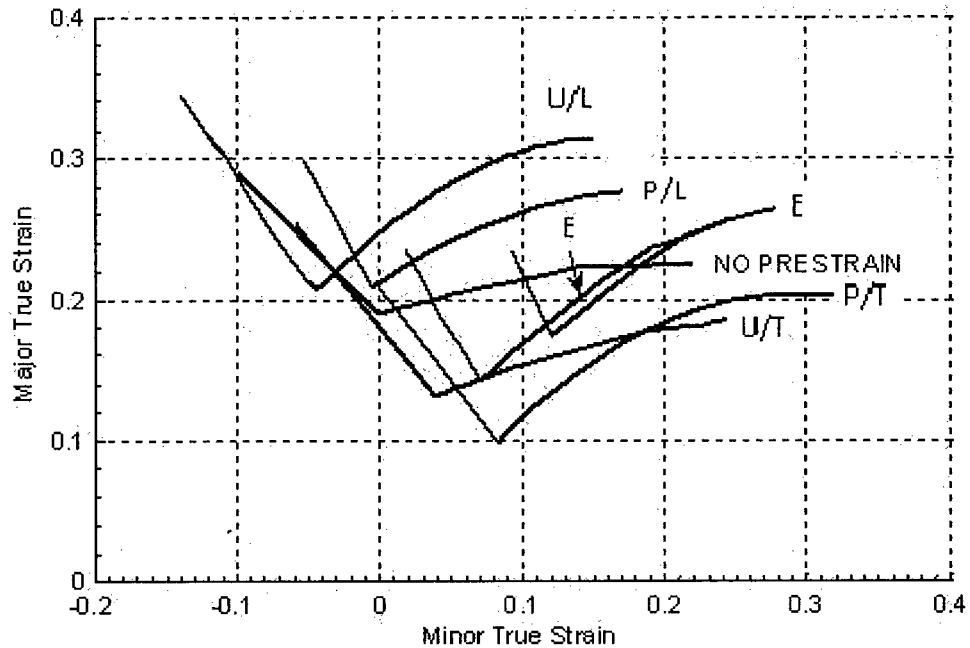


Figure 1-3: Strain-based Forming Limit Curves for various uniaxial (U), plane (P) and balanced biaxial (E) prestrains both longitudinal (L) and transverse (T) to the major strain direction for Al 2008-T4 [2]

To address this path dependence of the strain-based failure criterion, Stoughton [6] analytically converted 14 strain-based FLCs from Graf and Hosford to stress space and showed that an alternative stress-based forming limit criterion is less sensitive to changes in the strain path (see Fig. 1-4). Note that the 12% balanced biaxial prestrain case is an outlier possibly due to the higher prestrain value or experimental error. This path independence of the stress-based failure criterion would allow for more accurate prediction of tearing concerns during numerical simulations which would aid the design process.

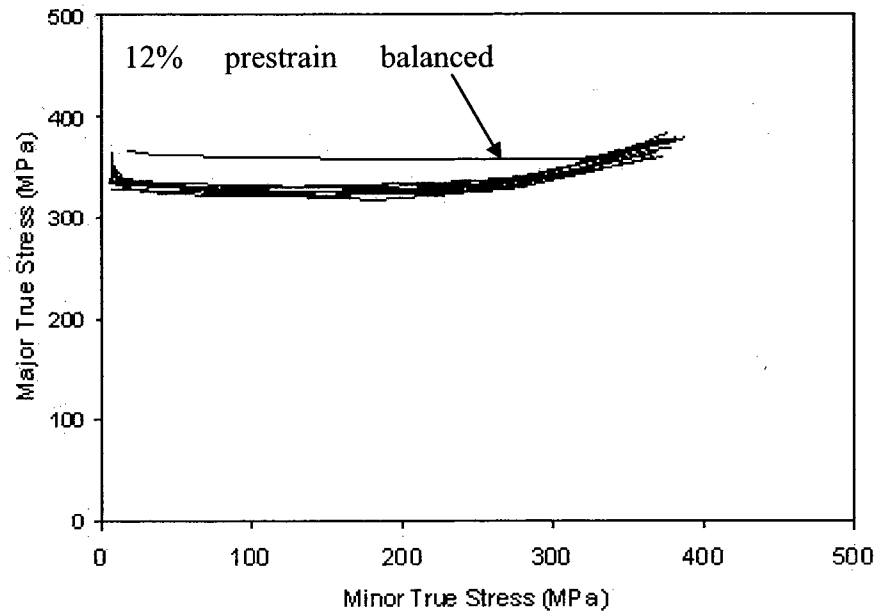


Figure 1-4: Fourteen strain-based FLCs from Graf and Hosford converge to one curve in stress space when analytically converted using Barlat's 1989 yield criterion [6].

Whether considering strain or stress-based FLCs, the experimental determination of the FLCs is time consuming and expensive. Therefore, theoretical methods to predict FLCs have been implemented. The most widely accepted approach to determine strain-based FLCs is the Marciniak and Kuczynski model (i.e., M-K model) [3]. This model assumes a material defect in the form of a region of decreased thickness (see Fig. 1-5). The orientation of this defect region (Region b) will vary based on the strain path assumed.

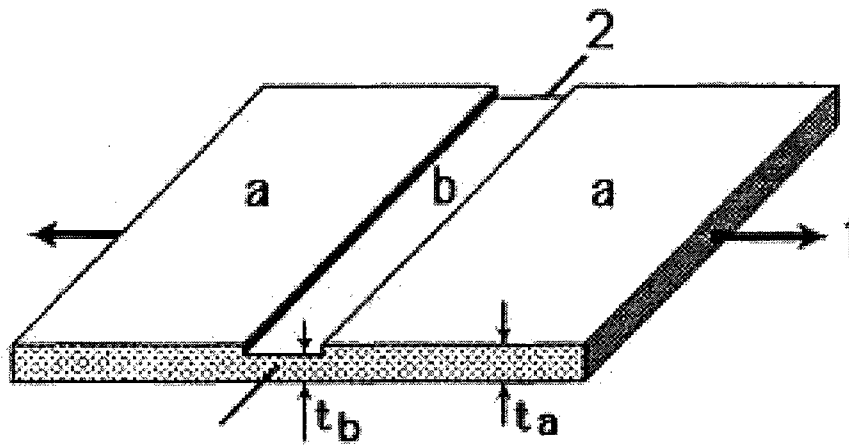


Figure 1-5: Schematic of safe (a) and defect (b) regions with varying thicknesses for the Marciniak and Kuczynski model [3].

For the M-K model, a strain path (and thus stress path), force equilibrium (e.g., in the 1-direction for Fig. 1-5), a yield criterion, and a constitutive relationship are assumed, and the strain increments in the safe (a) and defect (b) regions are predicted. A *key assumption* in the M-K model is the ratio of the strain increments when failure occurs (e.g., $\frac{\varepsilon_{1A}}{\varepsilon_{1B}} > 10$). Results show reasonable agreement with experimental data if accurate material parameters and yield criteria are used [7]. Furthermore, the shifting and distortion of the strain-based FLCs can be predicted if the prestrain is included in the analytical model [8].

Alternatively, Derov et al. [9] developed an analytical model to predict a stress-based FLD. This model predicts both stress and strain-based FLCs by assuming a constitutive relationship, yield criterion, and anisotropic parameters (R_0 and R_{90}) for the material. Similar to the M-K model, the Derov et al. model assumes a defect region in the material. However, instead of the decreased thickness region as in M-K model, a region of concentrated stress in the material is assumed for the defect region.

A *key assumption* in the Derov et al. model is the critical stress concentration factor, i.e., F-parameter, which represents the ratio of the effective stress in the “safe” region of the material to the effective stress in the “defect” region of the material. The F-parameter characterizes the failure condition for the material and is related to the material’s ability to work harden. See Appendix A for equations and details related to the Derov et al. model.

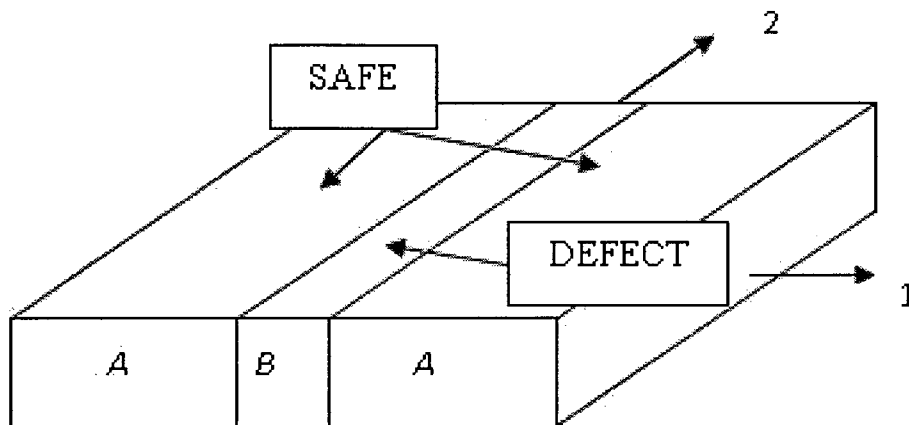


Figure 1-6: Schematic of the safe (A) and defect (B) regions for the Derov et al. model.

In this thesis, the key assumptions in the M-K and Derov et al. models are investigated for 1018 steel specimens using experimental data from Marciniak tests with coupled Digital Imaging Correlation (DIC) to measure the strain. In Chapter 2, the experimental set-up is presented. The implementation of the DIC system provided the detection of the strain concentrations during the experiments. The high strain concentration areas were determined using a strain contour plot, and a strain extraction grid was formed. Strains were obtained on these grid points inside (i.e., the defect region) and adjacent (i.e., the safe regions) to the high strain concentrations for eight different strain paths (i.e., specimen geometries). In Chapter 3, the incremental

strain ratio from the M-K model, the critical stress concentration factor from the Derov et al. model, and other parameters are investigated spatially and temporally. These results and graphs are discussed and compared with similar previous work which used experimental data obtained from National Institute of Science and Technology (NIST) for Al 6022-T4. Finally, conclusions (in Chapter 4) and future work (in Chapter 5) are presented.

CHAPTER 2

EXPERIMENTAL SET UP

Analytical predictions of forming limit curves are of interest; however, these theoretical models have to be experimentally investigated with respect to key assumption used. For this purpose, Marciniak tests with the Raghavan [10] modification were conducted on eight different geometries which produced varying strain paths from uniaxial to balanced biaxial. No lubrication was used for the tests. During the tests, digital images were obtained and analyzed using a Digital Imaging Correlation (DIC) system (i.e., Vic-3D 2009 from Correlated Solutions). The DIC system calculated strains in both the major and minor directions, and these strains were also converted to obtain the F-parameter for the Derov et al. model [9]. The strain contour plots allowed the defect and safe locations in the material to be identified.

2.1 Tooling and Specimen Geometries

During Marciniak tests, in-plane stretching is induced in the material through the Marciniak punch specimen geometries. For biaxial cases, the failure location is controlled with the help of a steel sacrificial washer. Binder plate forces and a lock ring are used to prevent any movement of the material into the forming area. As opposed to Nakajima tests where bending and friction are present; failure in the

central test region of Marciniak tests is dependent only on the material properties and imperfections.

Tests were conducted on eight different geometries varying the strain path from uniaxial to balanced biaxial. There are four main groups of specimens for the Raghavan modification identified with Roman (e.g., i for uniaxial and iv for balanced biaxial) (See Fig. 2-1). Raghavan modifications provide variations in the strain paths from uniaxial to balanced biaxial cases whereas Marciniak tests are only on balanced biaxial specimens [10]. Two tests were conducted for each specimen geometry. See Table 2-1 and Fig 2-2 for dimensions and schematics of specimens used in Marciniak tests.

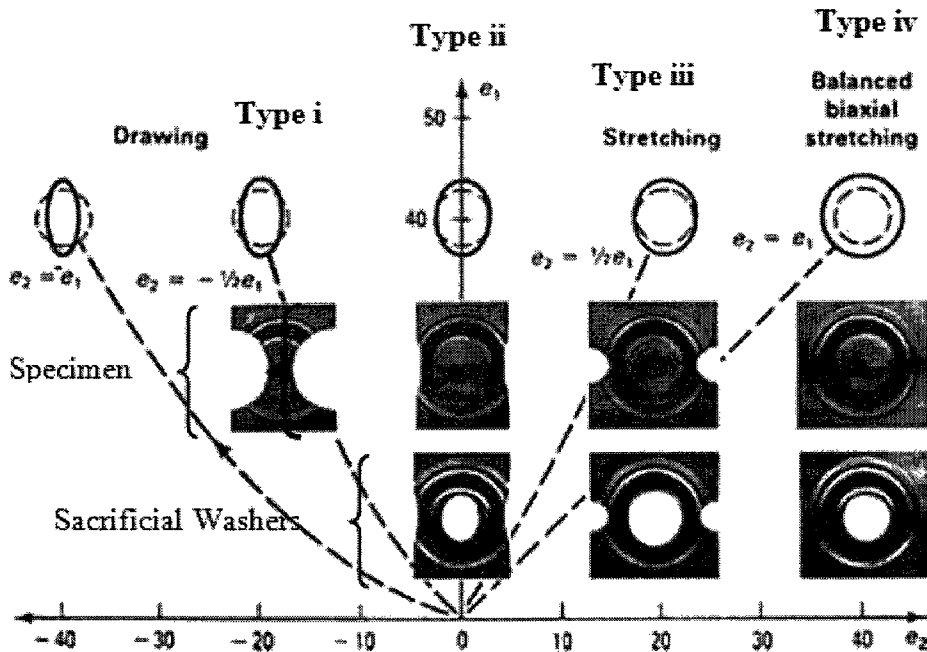
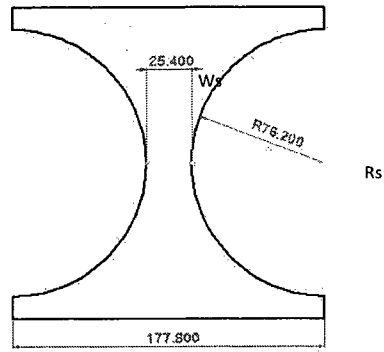
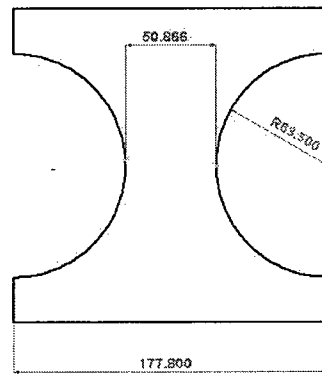


Figure 2-1: Representation of main groups of geometries for the Raghavan modification to Marciniak test.

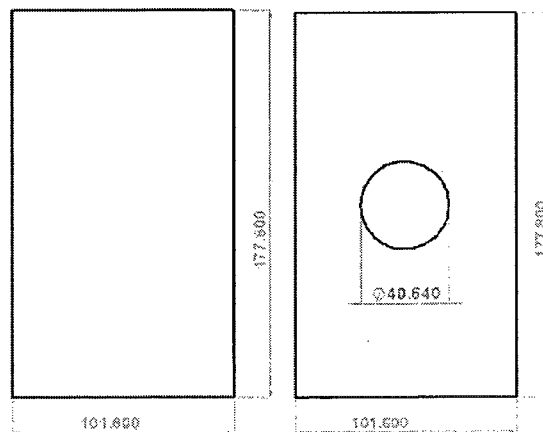
a)



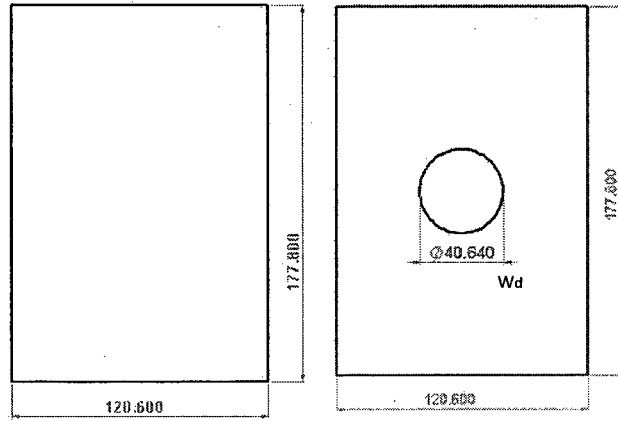
b)



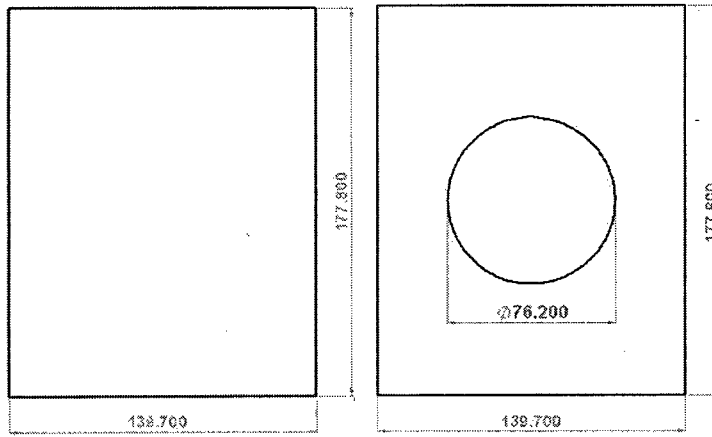
c)



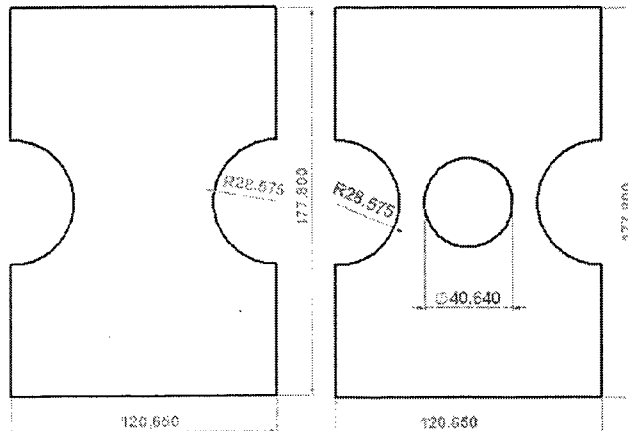
d)



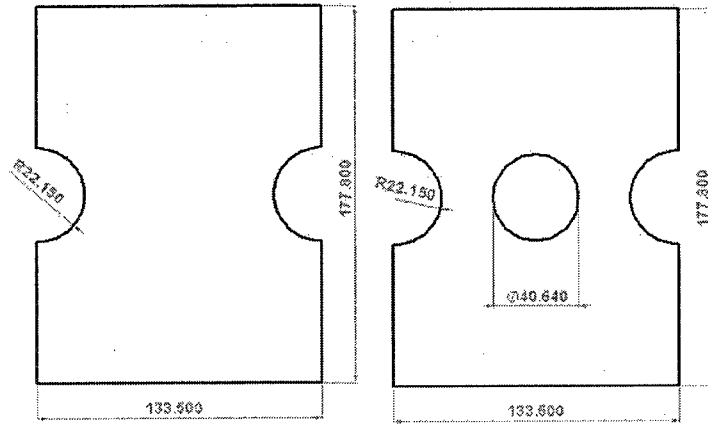
e)



f)



g)



h)

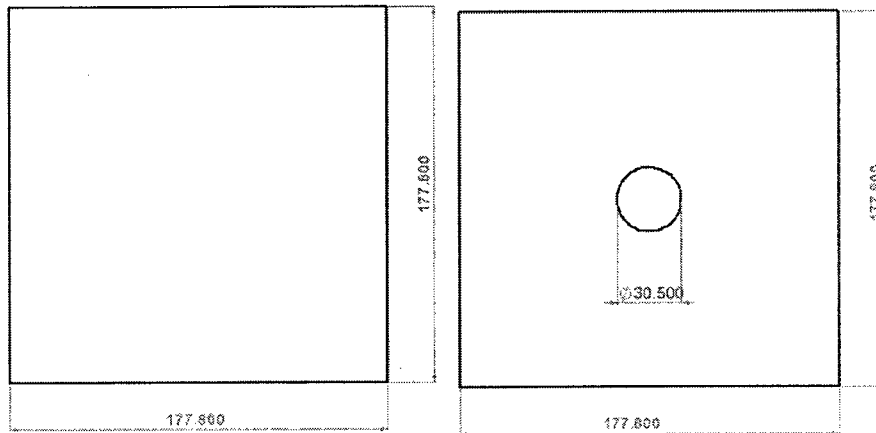


Figure 2-2: Schematic of various specimen (left) and washer (right) geometries for a) Type i1, b) Type i2, c) Type ii1, d) Type ii2, e) Type ii3, f) Type iii1, g) Type iii2 and h) Type iv specimens.

	Type ii	Type i2	Type iii	Type ii2	Type ii3	Type iiiii	Type iii2	Type iv
Width Ws (mm)	25.4	50.8	101.6	120.6	139.7	120.65	133.5	177.8
Notch Radius Rs (mm)	76.2	63.5	No notch			28.574	22.15	No notch
Washer Hole Diameter Wd (mm)	Nowasher		40.64	40.64	38.1	40.64	38.1	30.5

Table 2-1: Dimensions of the various specimen geometries.

2.2. Material Tested

The material used for both the specimen and sacrificial washer was 0.77mm (0.0305”) thick 1018 steel. Specimens and sacrificial washers were laser cut by Rapid Sheet Metal (Nashua, NH) to obtain the desired geometries. In order to characterize the material behaviour, in particular anisotropic effects, tensile tests were conducted. See Fig. 2-3 for stress versus strain data in three orientations with respect to the rolling direction (0, 45 and 90 degrees) and the curve fit for 0 degrees rolling direction. See Table 2-2 for material properties from the tests, assuming a power hardening law $\sigma = K\varepsilon^n$. Also, the anisotropic R-parameter which is the ratio of the width strain to the thickness strain (i.e., $R = \frac{d\varepsilon_w}{d\varepsilon_t}$) is provided in Table 2-2. The R-parameter values with respect to rolling direction ranged from 1.40-2.02. Similarly, the R-parameter values for another type of steel, HC220YD, used in Numisheet 2008 also had a similar range, from 1.28-2.08.

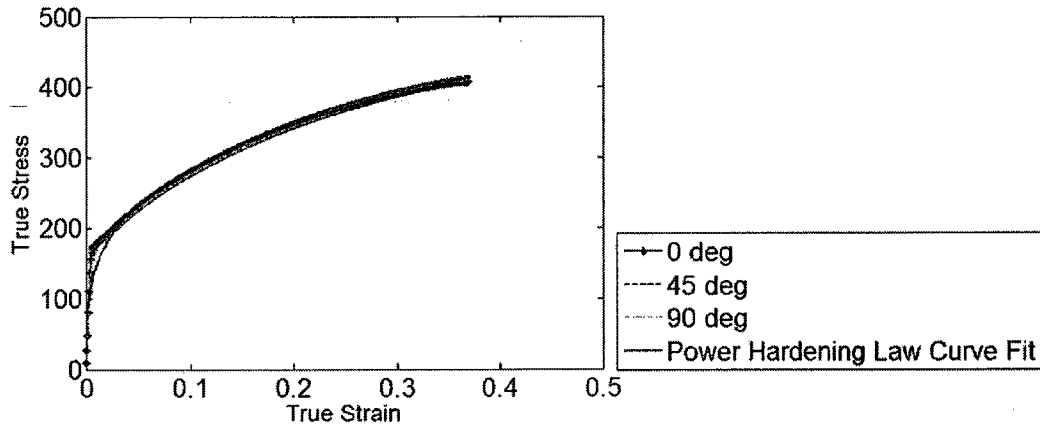


Figure 2-3: Tensile test data for 1018 Steel and power law curve fit for the 0 degree data.

Orientation to Rolling Direction (Degrees)	K (MPa)	n	R
0	549.16	0.28	2.02
45	547.02	0.29	1.87
90	538.77	0.29	1.40

Table 2-2: Material parameters for 1018 Steel used in Marciniak test [11].

2.3 Forming Press

The experiments were conducted on a 50 ton, 4 post hydraulic press with a central punch cylinder and 4 cylinders to produce the binder force (see Fig. 2-4). The hydraulic pump is a Rexroth pressure compensated axial piston pump rated for 8.57 GPM. Relief and proportional valves, which determined fluid pressure and flow respectively, were controlled using Labview software and an output card (National

Instruments NI-6703). The proportional valves are capable of 13 GPM flow. The tests were quasi-static with an approximate punch speed of 0.5 mm/sec. The process is not closed-loop controlled with respect to either pressure or velocity, but the resistance of the specimen based on a constant hydraulic system pressure determines the punch speed.

Punch and binder forces were measured using Transducer Techniques load cells with capacities of 62 kN (14000 lbs) and 111 kN (25000 lbs) respectively. In addition, punch displacement was measured using a Temposonic Linear Resistive Transducer (LRT) with a stroke length of 305mm (12 inches). The accuracy of this device is $\pm 0.01\%$ of full scale. Data was acquired through a Labview program and a NI-6033 data acquisition card.

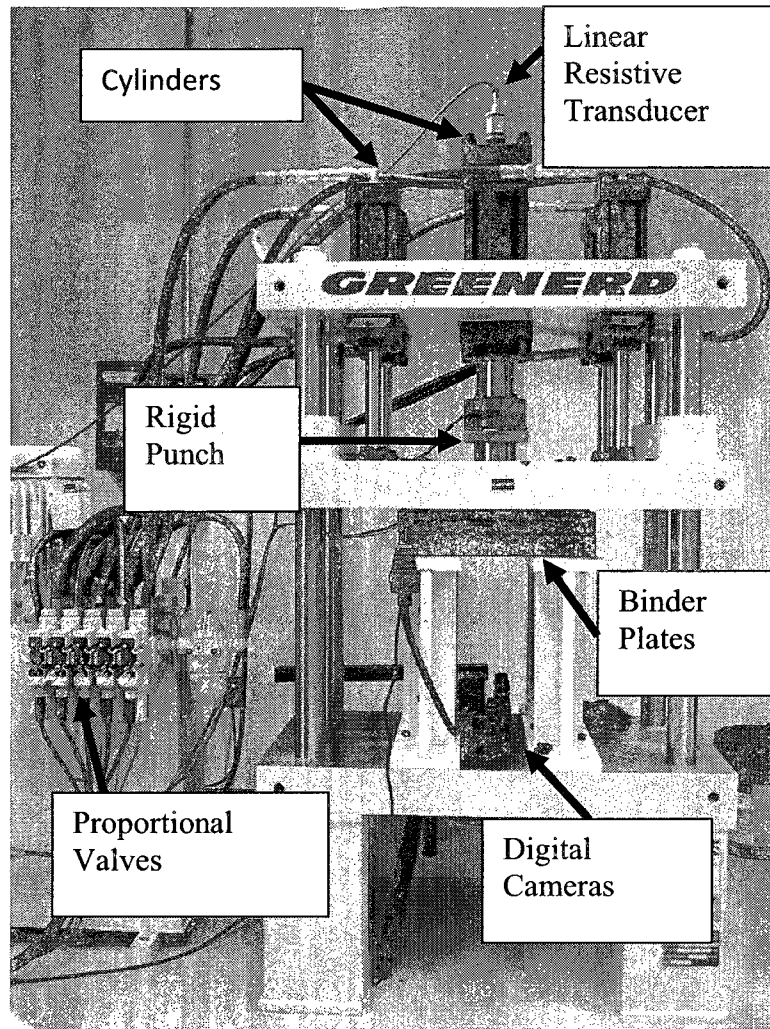


Figure 2-4: Experimental setup.

2.4 Digital Imaging Correlation System

In order to measure the deformation and in-plane strains during the tests, Digital Imaging Correlation (DIC) was used. With this technique, a speckle pattern is applied on the specimen, and this pattern is tracked using the digital images to determine the displacement, and thus strain, during the process. Although the Marciniak tests produce a plane stress condition in the central region of the specimen, a set up with two cameras was used in the process in order to capture out-of-plane deformation at the radius locations of the punch. The digital images were captured by two Point Grey

Digital Cameras (GRAS-20S4M-C) with 1200 x 1600 pixel resolution. The cameras were positioned with a separation angle of approximately 10° and controlled by the Vic-Snap software using the computer. After the images were obtained, Vic-3D DIC software was used to analyze the images. The sampling rate was set to one image per 0.1 second for biaxial specimens and 0.075 second for uniaxial specimens. Different sampling rates were chosen in order to keep the increments of strain to half a percent between the subsequent images and to capture sufficient data as the defect developed. The cameras were calibrated to establish intrinsic and extrinsic parameters to be used by the DIC software. The parameters are calculated by Vic-Snap automatically to determine the appropriate scale for image correlation and allow the speckles on the specimen surface to be located in a Cartesian coordinate system for analysis. The subset and step sizes were set to 21 and 5 respectively. These are the default values in Vic-3D software.

2.4.1 Preparation of the Specimen

A high contrast speckle pattern was applied on one side of the material to produce a uniform and randomly distributed pattern as required for DIC system [12]. As a preparation of the material, the surface was roughened using sand paper to promote the adhesion of the paint. Afterwards, the surface was chemically cleaned using a toluene, acetone and methanol based solution to remove any traces of dirt, oil and sand. To provide maximum adhesion, first a flat white primer was applied on the surface. Actual speckle contrast is created by covering the surface by spraying a base coat of flat white paint followed by an intermittent misting of flat black spray paint.

See Fig. 2-5 for an example of the speckle pattern applied to the specimen as viewed through the circular hole in the binder plate.

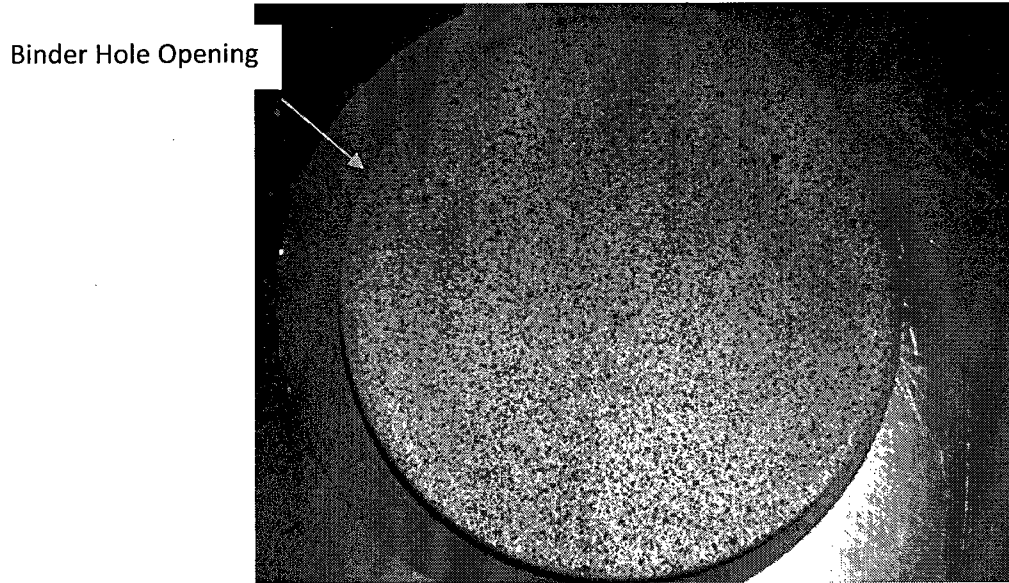


Figure 2-5: Speckle pattern on loaded specimen.

The misting of black paint was controlled by hand throttling the nozzle on the spray can at a distance of approximately 35cm to 40cm (approximately 14" to 16") away from the specimen. The approximate diameter of the resulting speckles varied from 0.23 mm to 2.8 mm (0.0118" to 0.1102") which provided between 2.5 and 30.5 pixels per speckle. This assured adequate resolution during subsequent testing and analysis. A stencil was made to mask the surface surrounding the area of interest to reduce the build-up of the paint that may adhere to binder plates during the test.

2.4.2 Post Processing of Digital Images

The major and minor in-plane strains were calculated from the correlation analysis using the Lagrange strain tensor. This is the default tensor for the strain calculations. The area of highest concentrated major strain was selected as the defect region. An

“Origin and X-Axis” coordinate system transformation was used to locate the origin at the point of highest concentrated major strain for the digital image directly before a physical tearing failure was observed (see Fig. 2-6). The direction of the defect region is identified by changing the scale of the contour plot and the X-axis is aligned on the perpendicular direction to this region. From this assumption, the Y- axis is assigned by the DIC system automatically.

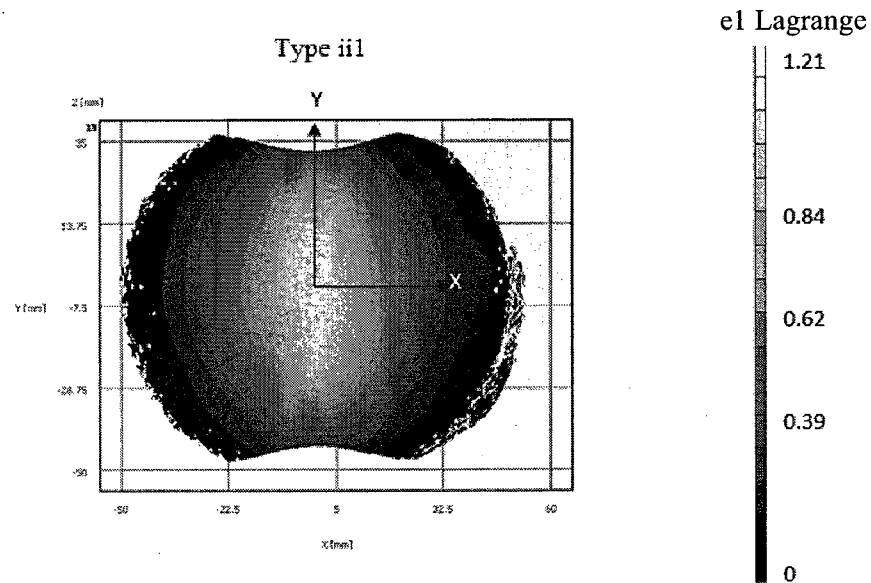


Figure 2-6: Contour plot for locating X- and Y- axis on the specimen

Following the coordinate transformation, strain data was obtained from the contour plots for use in three Matlab programs which distinguish between the safe and defect regions in the material and investigated the key assumptions in the M-K and Derov et al. models. For using in the first Matlab program, major and minor strain data were obtained from the DIC software at a series of 1mm-spaced nodes between ± 25 mm in the X-direction. This provided deformation data perpendicular to the defect as assumed in the M-K and Derov et al. models. A figure of the strain paths (major strain versus minor strain) for each node was created.

The second Matlab program was used to investigate the trend of the incremental major strain ratio with respect to forming depth. In the M-K model, failure is assumed to occur when the incremental strain in the defect region ($\Delta\varepsilon_{1a}$) is much larger than the incremental strain in the safe region ($\Delta\varepsilon_{1b}$), e.g.:

$$\Delta\varepsilon_{1a} < \frac{1}{10} \Delta\varepsilon_{1b} \quad (2.1)$$

or a similar ratio. For all images in the test, the program compared the change in incremental strain between images at the defect node to that of the four nodes perpendicular to the defect orientation ($\Delta\varepsilon_{1b} / \Delta\varepsilon_{1a}$). This served to identify the safe and defect regions as well as to investigate the validity of Eq. 2.1. The strain ratio plots will be presented in Chapter 3.

The third Matlab program was used to distinguish the safe and defect regions by investigating how the critical stress concentration factor (i.e., the F-parameter) from the Derov et al. model varied spatially and temporally. To obtain data for this program, an X-Y grid was created over the major strain contour plot. This grid was centered over the assumed defect and had 1mm spacing in both the X- and Y-directions (see Fig. 2-7). The grid size was chosen to cover the largest area possible while still remaining within the area of in-plane deformation.

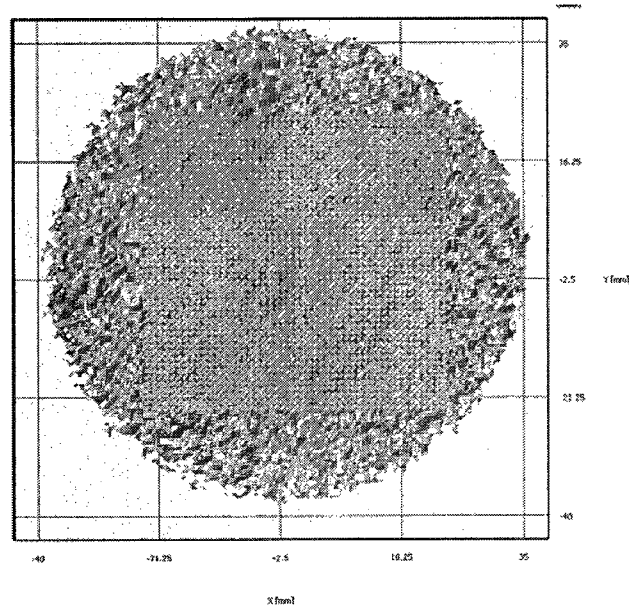


Figure 2-7: An example of a grid of extracted nodes on the specimen.

Major and minor strain data was then obtained from the DIC software at these points for the image immediately before fracture and from 4 previous images spaced in ten-frame increments (i.e., images that are 1, 2, 3, and 4 seconds prior to the failure image for Type ii, iii and iv specimens and 0.75, 1.5, 2.25 and 3 seconds prior to failure for Type i specimen). The Matlab program first determined the point of highest major strain in the grid, i.e., the defect node, and then used this as a reference for calculating the critical stress concentration factor (i.e., F-parameter) at each node based on the corresponding strain values.

The major and minor Lagrangian strain values determined for the defect node (i.e., e_{1B} and e_{2B}) and the safe region, (i.e., e_{1A} and e_{2A}) were first converted to true strains (i.e., ϵ_{1B} , ϵ_{2B} and ϵ_{1A} , ϵ_{2A}) using:

$$\epsilon = \frac{1}{2} \ln (1 + 2e_L) \quad (2.2)$$

Note that Eq. 2.2 is used as an approximation for the true strain values. More investigation is needed to assure this conversion between Lagrangian and true strains is correct for this two-dimensional case. The “safe” region refers to the area outside the defect node. From these values, the strain ratio of minor true strain to major true strain (i.e., $\rho = \frac{\varepsilon_2}{\varepsilon_1}$) was calculated. The stress ratio which is defined as the ratio of minor true stress to major true stress (i.e., $\alpha = \frac{\sigma_2}{\sigma_1}$) was calculated based on the ρ value assuming Hill’s 1948 yield criterion [13]:

$$\alpha = \frac{(1+\frac{1}{R_0})\rho+1}{\rho+(1+\frac{1}{R_0})} \quad (2.3)$$

A strain ratio (ρ) and stress ratio (α) were calculated for every node. A critical stress concentration factor, F-parameter, was then determined for all nodes. Assuming Hill’s 1948 yield criterion and that the stress normal to the sheet in the thickness direction, σ_3 , is negligible, the effective stress, $\bar{\sigma}$, and major true stress, σ_1 , are related by:

$$\frac{\bar{\sigma}}{\sigma_1} = \sqrt{1 + \left(\frac{1+R_0}{R_0}\right) \left(\frac{R_0}{1+R_0}\right) \alpha^2 - \left(\frac{2R_0}{1+R_0}\right) \alpha} \quad (2.4)$$

This expression was then applied to both the defect and safe regions of the material, and a ratio was created:

$$\frac{\frac{\bar{\sigma}_A}{\sigma_{1A}}}{\frac{\bar{\sigma}_B}{\sigma_{1B}}} = \frac{\sqrt{1 + \left(\frac{1+R_0}{R_0}\right) \left(\frac{R_0}{1+R_0}\right) \alpha_A^2 - \left(\frac{2R_0}{1+R_0}\right) \alpha_A}}{\sqrt{1 + \left(\frac{1+R_0}{R_0}\right) \left(\frac{R_0}{1+R_0}\right) \alpha_B^2 - \left(\frac{2R_0}{1+R_0}\right) \alpha_B}} \quad (2.5)$$

By multiplying both sides of Eq. 2.5 by the ratio of the major true stresses in the safe and defect regions, the definition of the critical stress concentration factor, or F-parameter, becomes:

$$F = \frac{\bar{\sigma}_A}{\bar{\sigma}_B} = \frac{\sqrt{1 + \left(\frac{1+R_{90}}{R_{90}}\right)\left(\frac{R_0}{1+R_0}\right)\alpha_A^2 - \left(\frac{2R_0}{1+R_0}\right)\alpha_A}}{\sqrt{1 + \left(\frac{1+R_{90}}{R_{90}}\right)\left(\frac{R_0}{1+R_0}\right)\alpha_B^2 - \left(\frac{2R_0}{1+R_0}\right)\alpha_B}} * \frac{\sigma_{1A}}{\sigma_{1B}} \quad (2-6)$$

The ratio of major true stresses in the safe and defect regions can be equated to the respective true strains by considering force balance in the major direction, i.e., perpendicular to the defect (see Fig. 1-5), which must exist in these regions:

$$Force_{1A} = Force_{1B} \quad (2.7)$$

$$\sigma_{1A}Area_{1A} = \sigma_{1B}Area_{1B} \quad (2.8)$$

Assuming that the respective widths of $Area_{1A}$ and $Area_{1B}$ are equal, Eq. 2.8 can be reduced to:

$$\sigma_{1A}t_{1A} = \sigma_{1B}t_{1B} \quad (2.9)$$

where t_{1A} and t_{1B} are the instantaneous thicknesses of the safe and defect regions respectively. Assuming the same initial thickness exists prior to forming, these two quantities can be related by the thickness strains, ϵ_{3A} and ϵ_{3B} . Assuming conservation of volume exists in the safe and defect regions throughout the forming process:

$$t = t_0 \exp^{-\varepsilon_3} = t_0 \exp^{-\varepsilon_1 - \varepsilon_2} \quad (2.10)$$

By applying Eq. 2.10 to both the safe and defect regions and substituting it into Eq. 2.9:

$$\frac{\sigma_{1A}}{\sigma_{1B}} = \frac{\exp^{-\varepsilon_{1B} - \varepsilon_{2B}}}{\exp^{-\varepsilon_{1A} - \varepsilon_{2A}}} \quad (2.11)$$

Finally, by substituting Eq. 2.11 into Eq. 2.6, the critical stress concentration factor, i.e., F-parameter can be expressed as:

$$F = \frac{\sqrt{1 + \left(\frac{1+R_{90}}{R_{90}}\right) \left(\frac{R_0}{1+R_0}\right) \alpha_A^2 - \left(\frac{2R_0}{1+R_0}\right) \alpha_A}}{\sqrt{1 + \left(\frac{1+R_{90}}{R_{90}}\right) \left(\frac{R_0}{1+R_0}\right) \alpha_B^2 - \left(\frac{2R_0}{1+R_0}\right) \alpha_B}} * \frac{\exp^{-\varepsilon_{1B} - \varepsilon_{2B}}}{\exp^{-\varepsilon_{1A} - \varepsilon_{2A}}} \quad (2.12)$$

Thus, only the strain data obtained from the DIC software is required to calculate the critical stress concentration factor.

After performing these calculations, the program generated a surface plot of the F-parameter versus X- and Y-location for the data obtained from the image just prior to the tearing failure. In addition, the program generated for each image a line plot of the F-parameter versus X- location from the defect node, using the row of perpendicular nodes passing through the defect node. Again, this was done to correspond to the assumption in the Derov et al. model regarding the location and orientation of the safe and defect regions. These two plots provide spatial and temporal data of the critical stress concentration factor to define the safe and defect regions.

Note that the load and displacement data for the punch were also obtained but were not analyzed in detail. However, these results did not show any abnormal discontinuities during the test or with respect to the DIC analysis.

In addition, the reliability of DIC measurements was verified by measuring the distance between two speckle points on both an actual, physical specimen using callipers and in the DIC software. See Fig. 2-8. Approximately the same distance was obtained (i.e., 22.5 mm for the physical measurement and 21.5 mm using the tools in the Vic-3D software). While not an exact match was obtained due to measurement error and possibly not selecting the exact speckles, these measurements provide confidence in the data obtained from the DIC software.

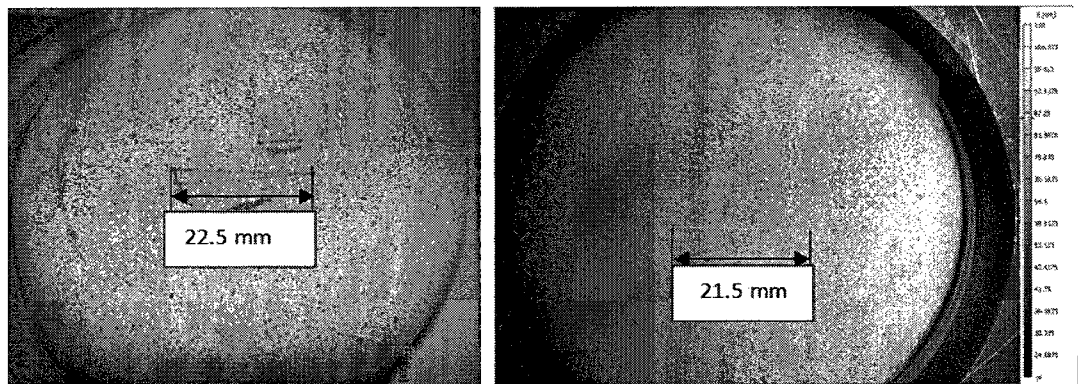


Figure 2-8: Pictures of a) physical and b) DIC system measurements for comparison

CHAPTER 3

EXPERIMENTAL RESULTS

In this chapter, the results of the Marciniak tests for different geometries are presented with respect to the key assumptions in the M-K model (i.e., the incremental strain ratio reaching a critical value) and the Derov et al. model (i.e., the critical stress concentration factor). As expected, the various specimen geometries produced a distribution of strain paths varying from uniaxial to balanced biaxial (see Fig. 3-1). Note that Types i2 and ii1 are redundant with Type i1 at lower major strain values. Similarly, Type iii1 is redundant with Type ii3. For figures comparing the various strain paths in this chapter, the specimen types connected by a line are Types i1, ii2, ii3, and iv as these provided the largest range of strain paths and consistent trends. The data for the other specimen types is also provided as points.

For example as shown in Fig. 3-2, with increasing initial strain path (i.e., $\rho = \frac{\Delta\epsilon_2}{\Delta\epsilon_1}$ which was taken at an approximate major strain of 0.1 and increases theoretically from -0.5 for uniaxial to 1 for balanced biaxial), the trend is for the forming depth to reach failure to increase due to more material resisting deformation (see Fig. 2-2 for the specimen geometries). The specimen types that did not follow this trend well are Types i2, ii1, iii1 and iii2. Recall that the sacrificial washer is not used for Type i specimens. The sacrificial washer significantly increased the forming depth at failure for Type ii specimens compared to Type i specimens.

For Types iii1 and iii2 specimens, the cause of not following the forming depth trend is that the failure locations were near the hole edge location on the sacrificial washer. See Fig. 3-3 that shows contour strain plots for all of the geometries investigated. Type ii3 specimens also failed near the hole edge location on the sacrificial washer, but the data followed the expected trend for forming depth and the key assumptions in the analytical models which will be shown in the following sections. Also note from the contour plots that Type iv specimens had an abnormal shaped area of concentrated strain (i.e., three “lobed” area) due to the balanced biaxial stretching that was induced. Finally, using the strain values of different geometries, an approximate strain-based FLD for the 1018 steel used in these experiments was defined (see Fig. 3-4). To create this figure, data from Types i1, ii2, ii3 and iv specimens were used since the strain paths of these specimen were neither redundant nor did the specimens fail near the hole edge of the sacrificial washer.

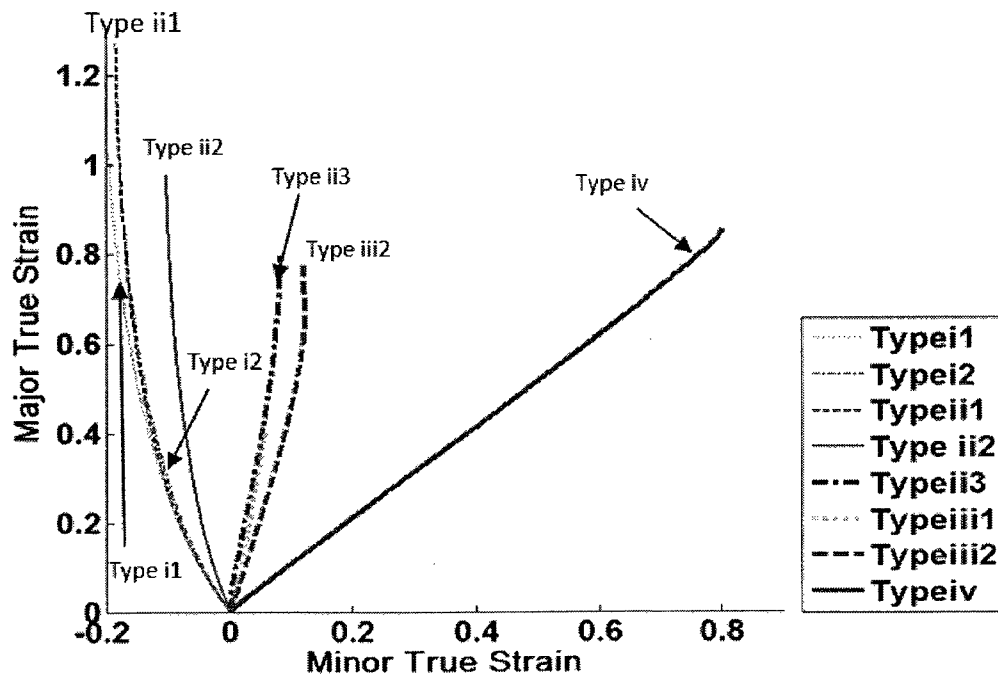


Figure 3-1: Strain paths varying from uniaxial to balanced biaxial cases for the various specimen types.

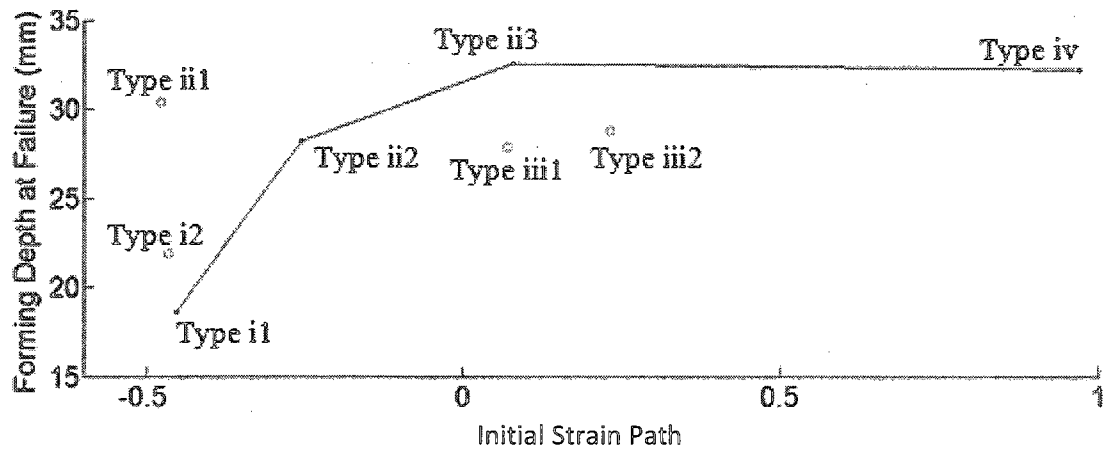
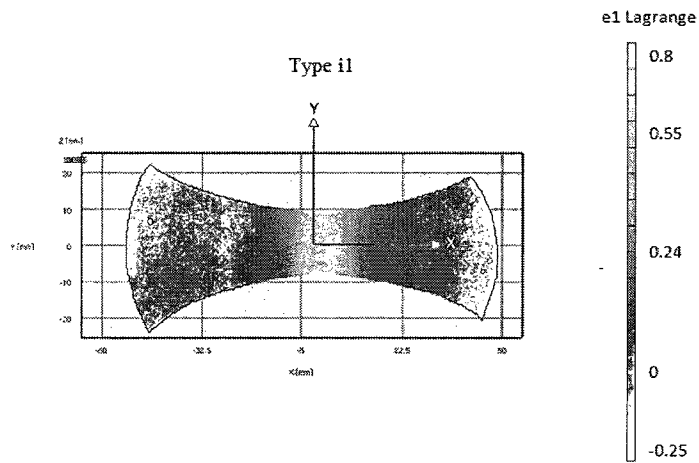
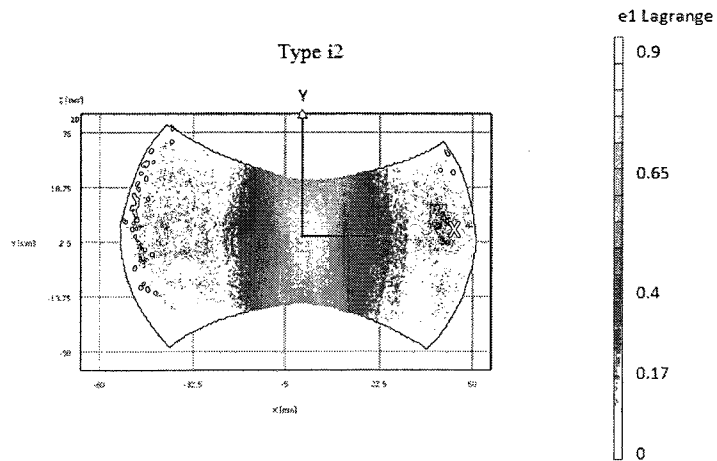


Figure 3-2: Initial strain path ($\frac{\Delta\epsilon_2}{\Delta\epsilon_1}$) versus forming depth at failure.

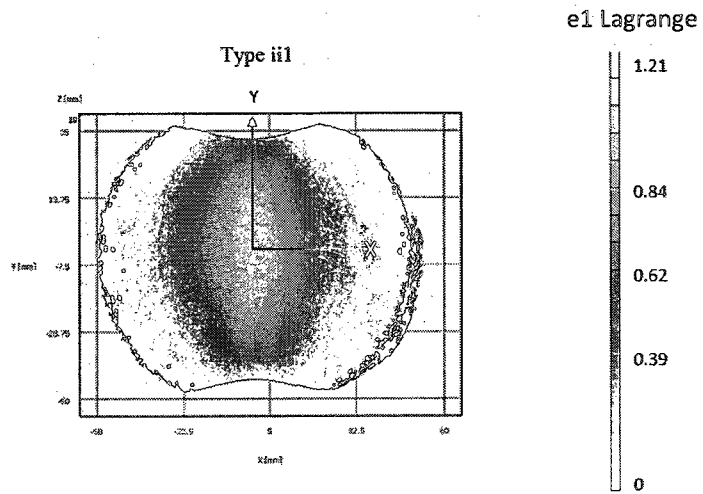
a)



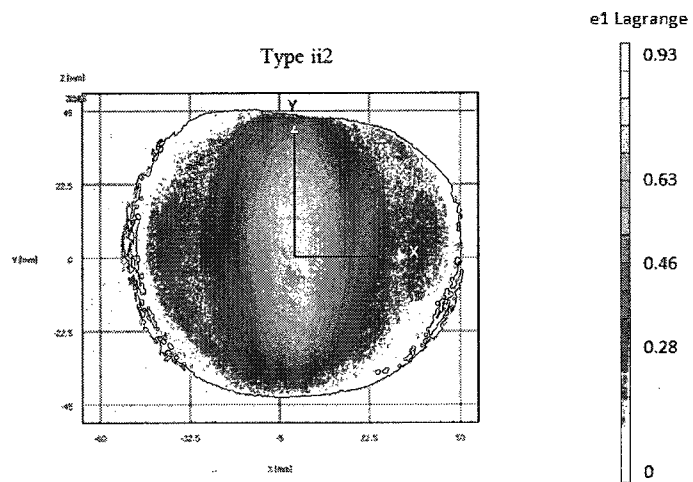
b)



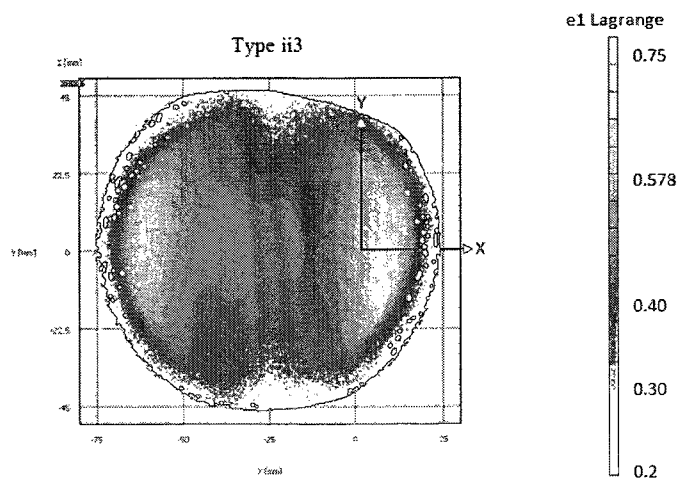
c)



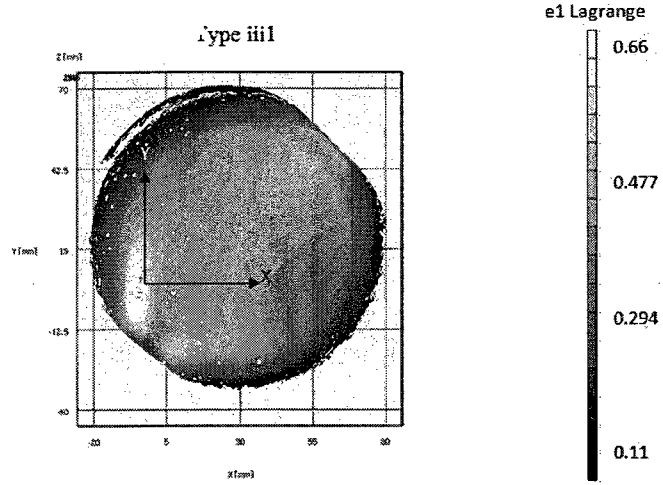
d)



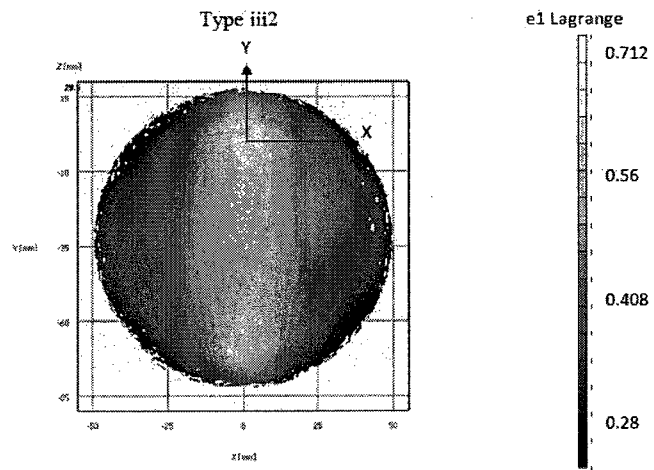
e)



f)



g)



h)

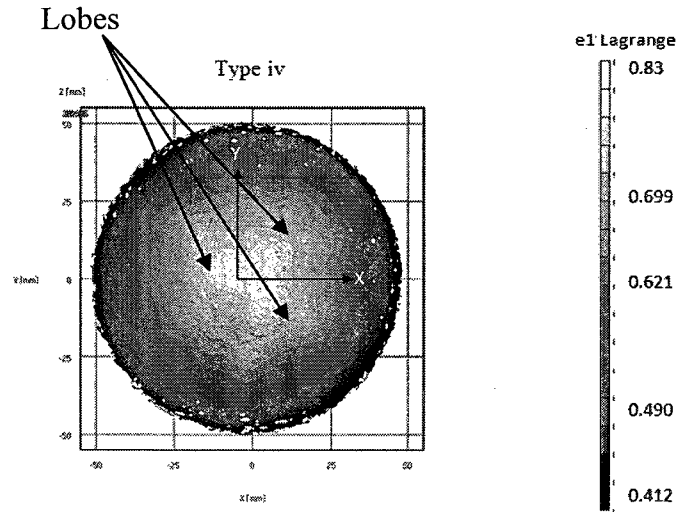


Figure 3-3: Contour plots of major strain with defect orientations shown for a) Type i1, b) Type i2, c) Type ii1, d) Type ii2, e) Type ii3, f) Type iii1, g) Type iii2 and h) Type iv specimens.

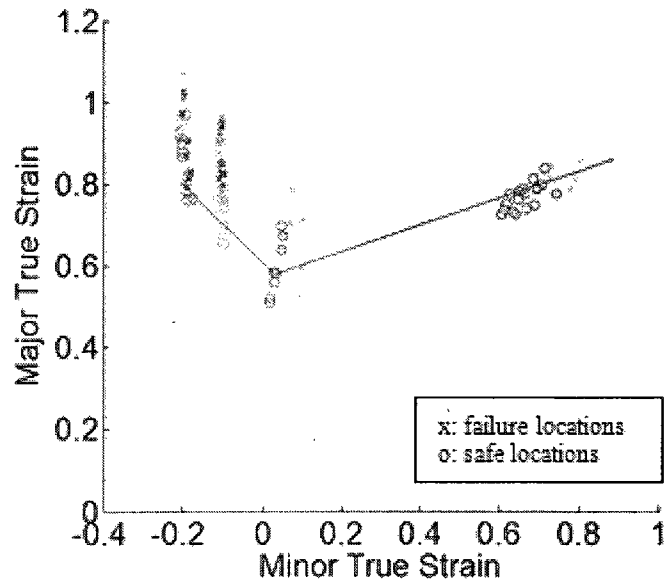


Figure 3-4: Strain-based Forming Limit Diagram for Steel 1018 from the experimental data for Type i1, ii2, ii3 and iv specimens.

3.1 Results for M-K Model Key Assumption

The M-K model assumes a narrow defect region on the specimen in which the thickness is assumed to be thinner than the safe region. The strain paths for the node (i.e., location) with the highest major strain value were defined as the defect. Figure 3-3 shows the defect region orientations and perpendicular axis directions for all specimen types. To define the safe region, the strains at the nodes at distances of 2, 5 and 10 mm perpendicular to the defect in the X- direction are plotted for different specimen types in Fig. 3-5.

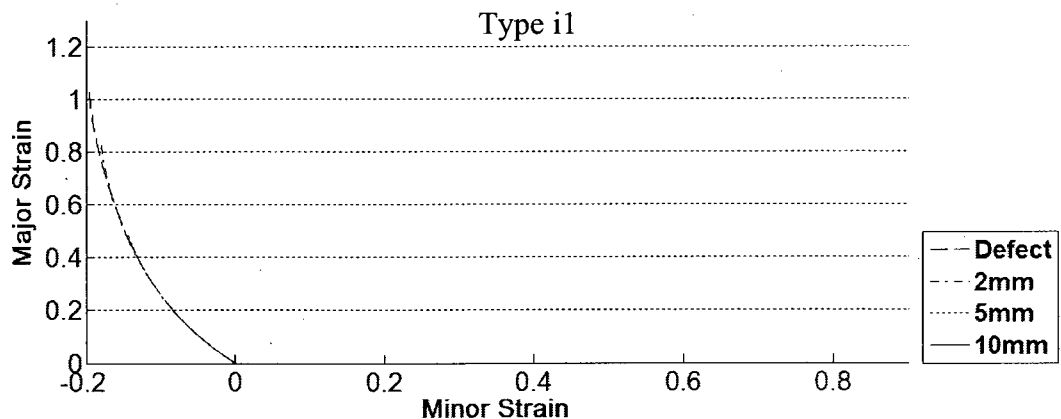
Conceptually, the divergence of the strain path curves for the defect location in the M-K model should occur as observed in the two specimen types with positive minor strain and the safe region 5 mm away (see Figs. 3-5 g) and h)). That is, the defect and safe regions follow the same strain path but then the defect region curve diverges just prior to failure. Note that the divergence of the 10 mm away from the defect location curves occurred early in the deformation process due to the localization of the defect region.

For the uniaxial cases (i.e., Figs. 3-5 a) through c)), note that even 10 mm away from the defect region, the divergence was not observed and the defect and safe regions follow the same strain path throughout the process even up to failure. However if the defect location and 5 mm away from the defect location is investigated with respect to time index for Type i1, Fig. 3-6 shows that the strain at 5mm diverged and had less major strain than the defect location at the time of failure. For the plane strain case in Fig. 3-5 f) for Type ii3 specimens, even at low major strain values, the strain path

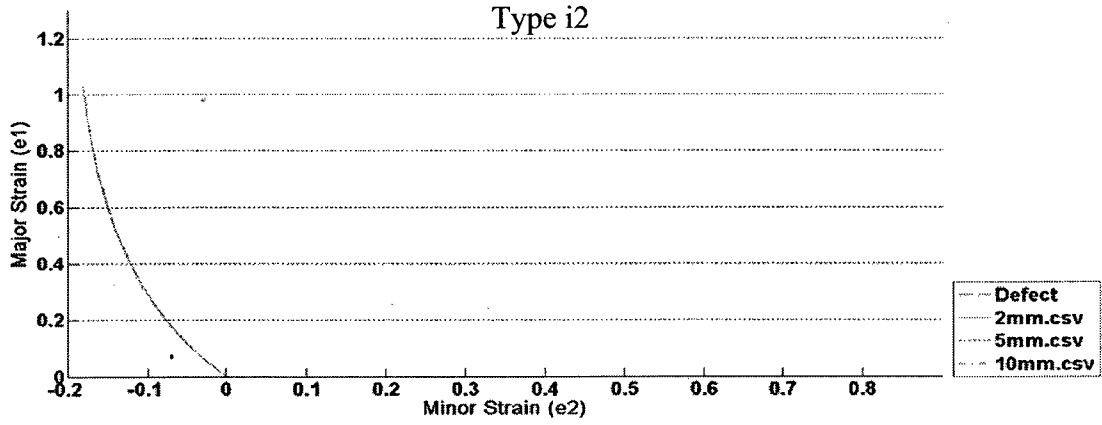
deviates for the defect and various locations, while for Fig. 3-5 e) for Type iii1 specimens, the strain paths are nearly plane strain throughout.

Figure 3-7 shows the incremental strain ratio $\left(\frac{\Delta\varepsilon_{1b}}{\Delta\varepsilon_{1a}}\right)$ for all of the specimen types with respect to the defect node and the location 5 mm away in the X-direction. As the initial strain path increases, the incremental strain ratio for the image directly before the tearing failure was observed decreased (e.g., approximately 12 for the uniaxial Type i1 case and 2.5 for Type iv balanced biaxial case) (see Fig. 3-7). Thus, the incremental strain ratio is not a constant value which is often assumed when implementing the M-K model. However, the line trajectory just prior to failure in Fig. 3-7 is nearly vertical, thus indicating the localization of the deformation in the defect region. Note as in Fig. 3-2, the redundant specimen geometries (i.e., Type i1 and ii1 specimens) and those that failed at the hole edge of the sacrificial washer (i.e., Type iii1 and iii2 specimens) are shown as points and do not follow the trend in Fig. 3-8.

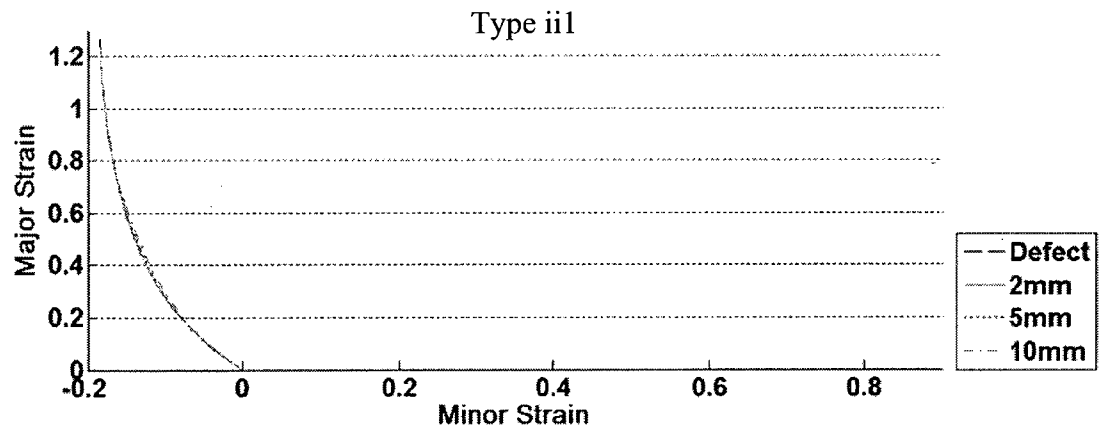
a)



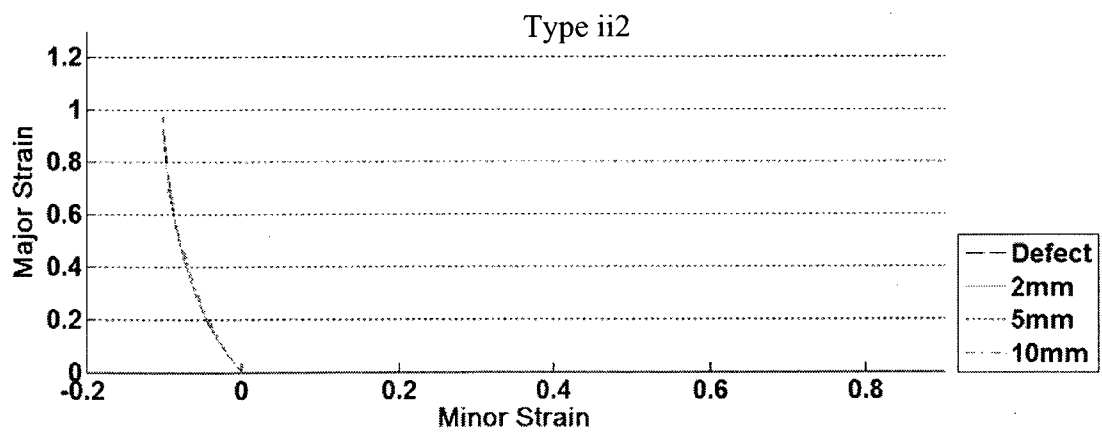
b)



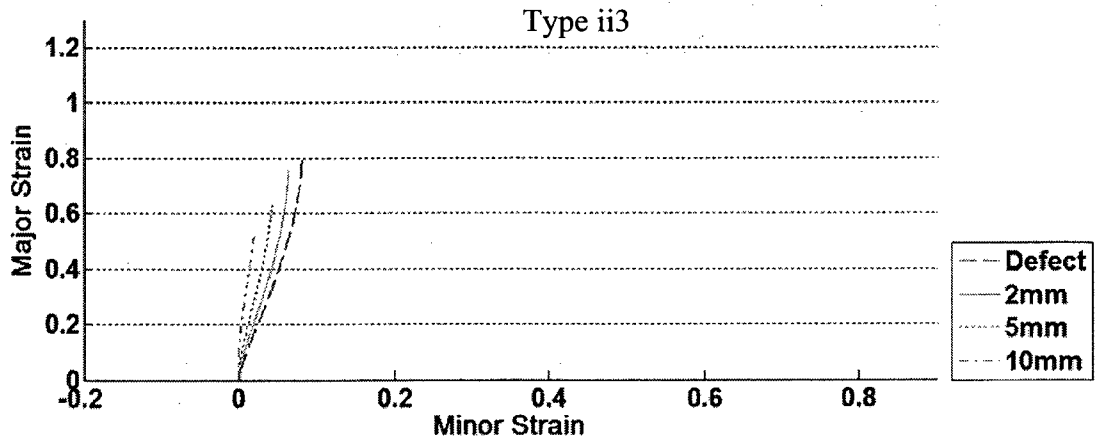
c)



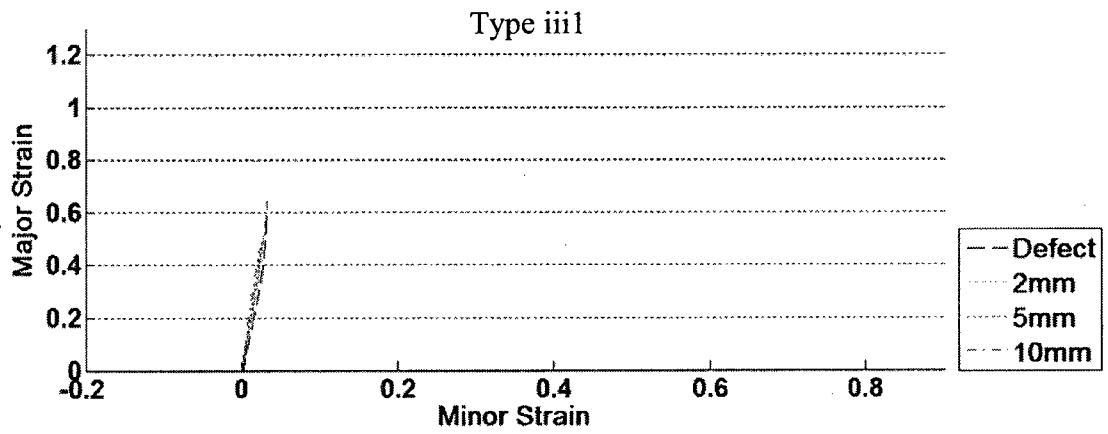
d)



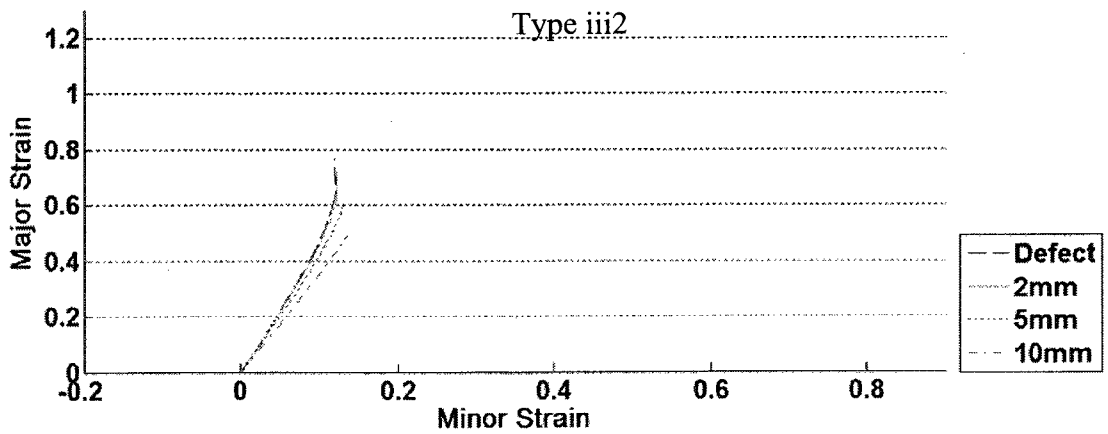
e)



f)



g)



h)

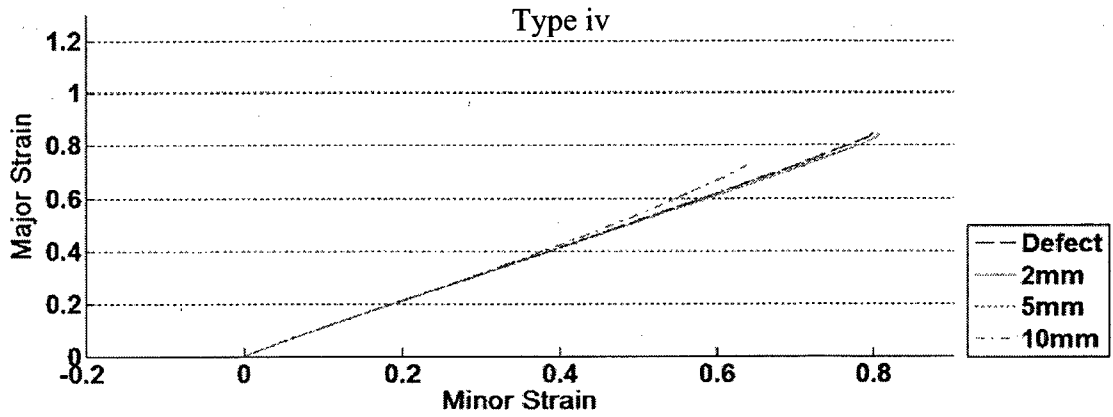


Figure 3-5: Strain path curves for the defect node and locations at 2, 5 and 10 mm away in the X-direction for a) Type i1, b) Type i2, c) Type ii1, d) Type ii2, e) Type ii3, f) Type iii1, g) Type iii2 and h) Type iv specimens.

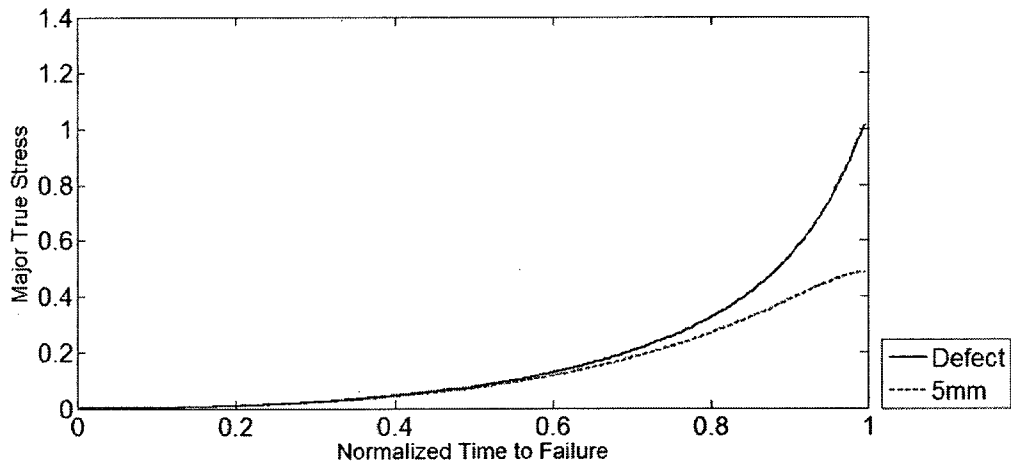
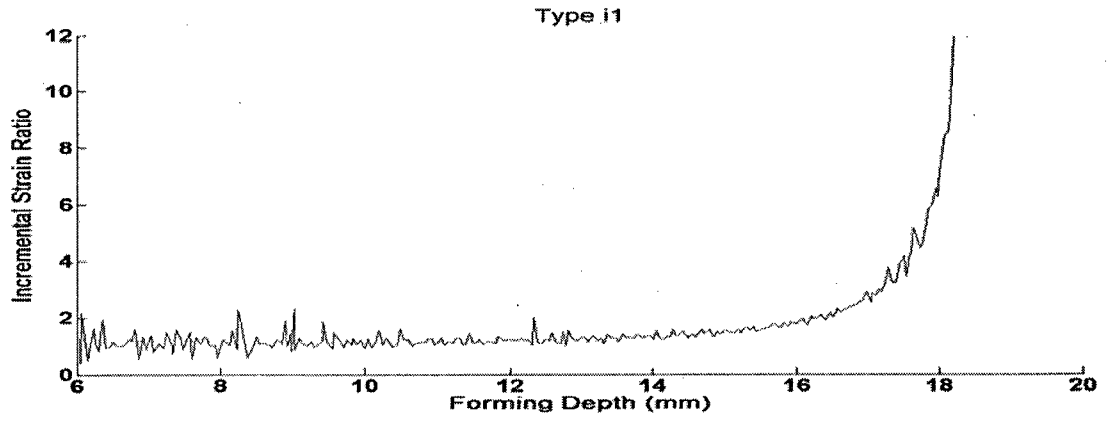
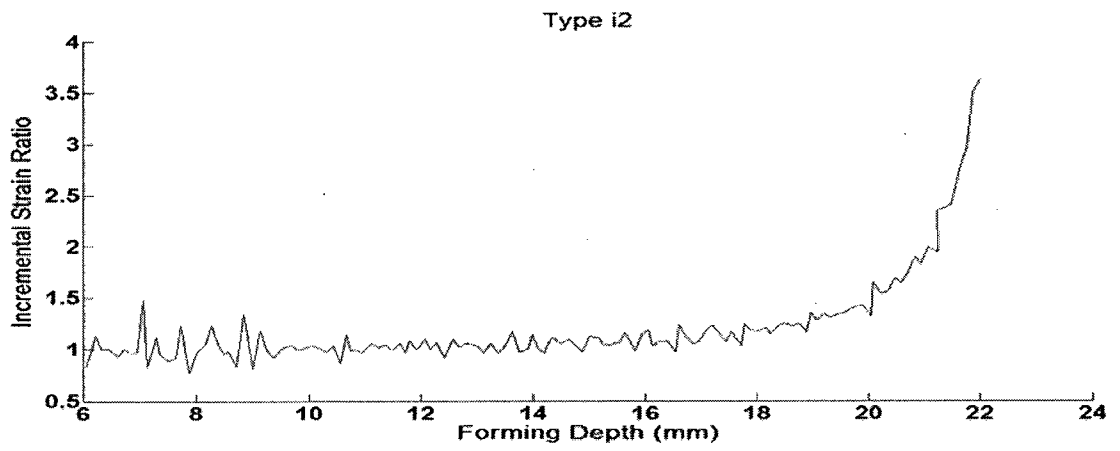


Figure 3-6: Major true strain for Type i1 specimen for defect node and node 5 mm away versus normalized time to failure.

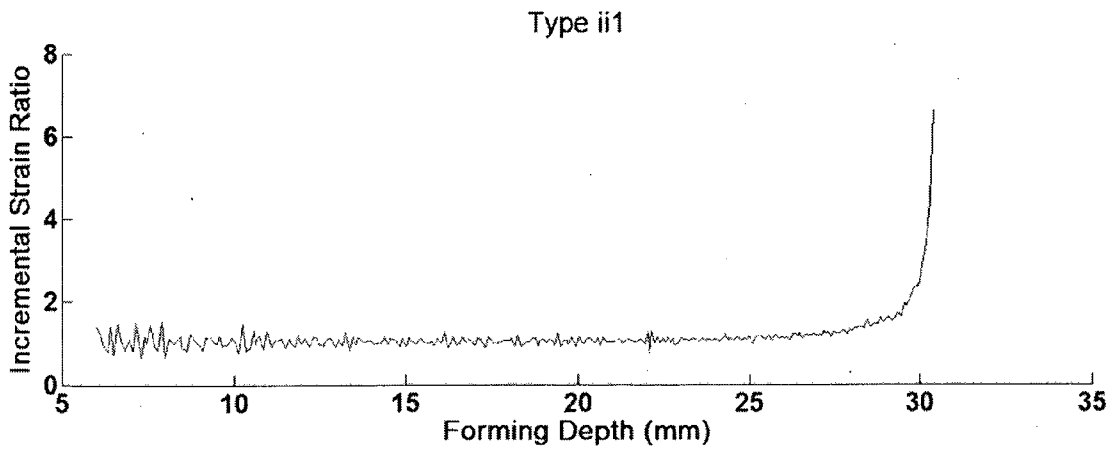
a)



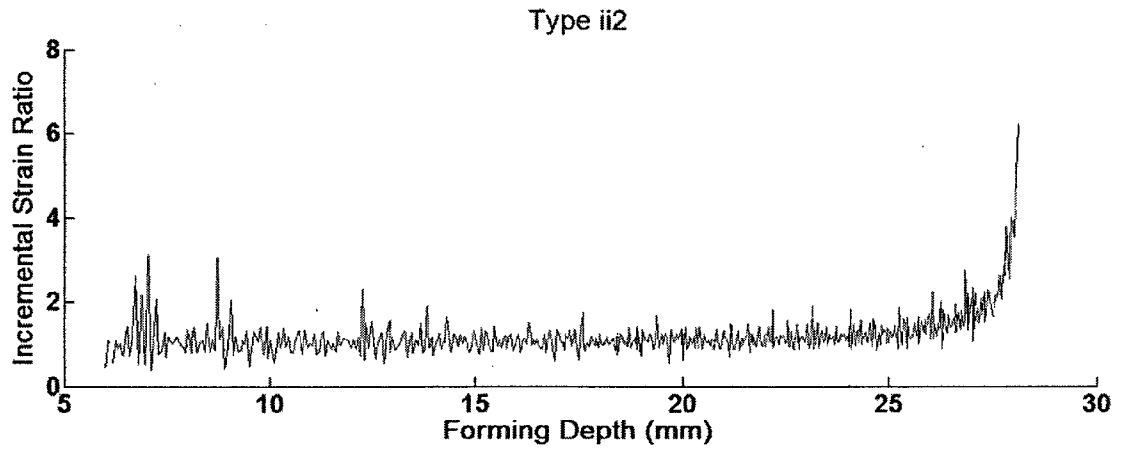
b)



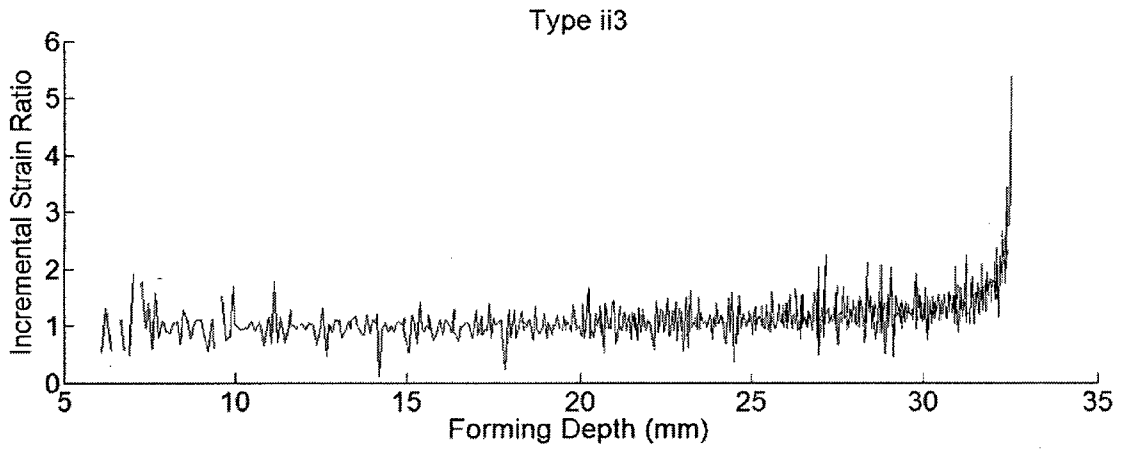
c)



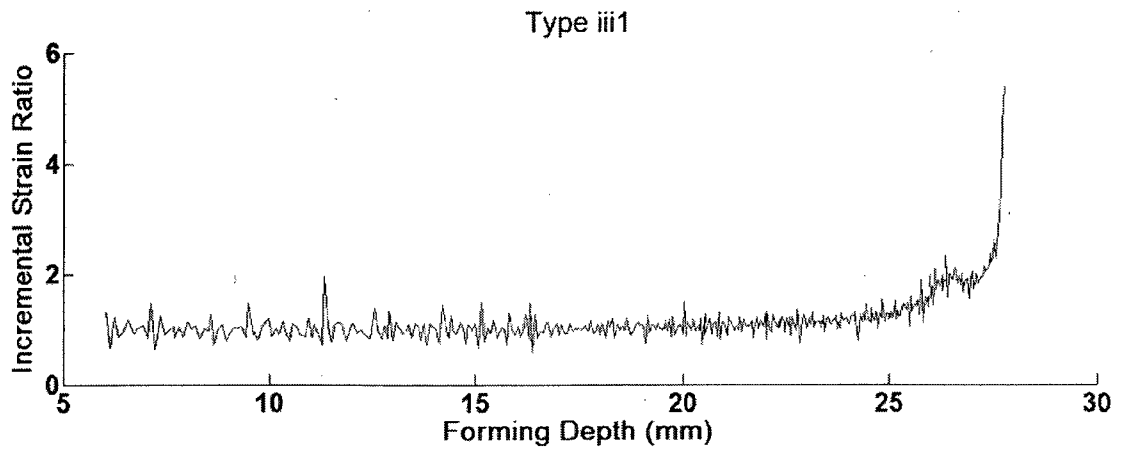
d)



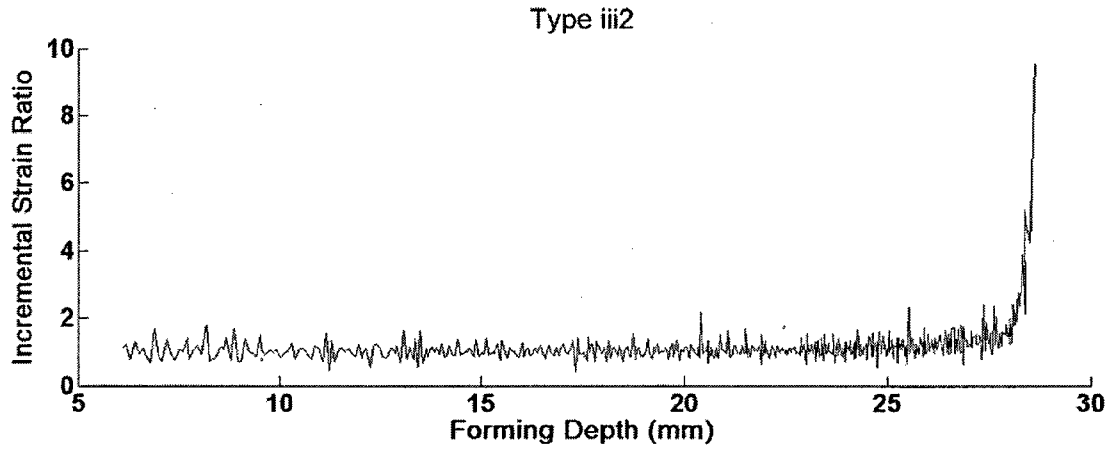
e)



f)



g)



h)

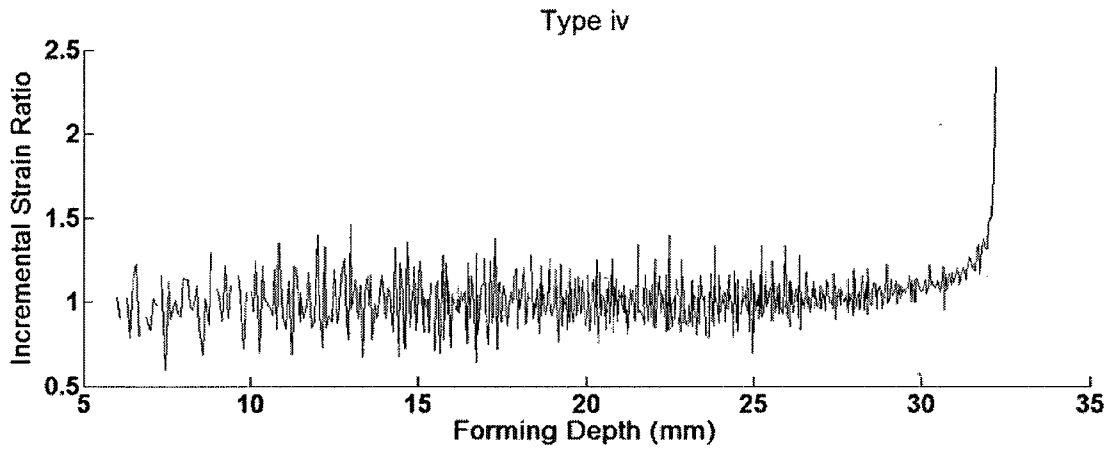


Figure 3-7: Incremental strain ratios versus forming depth for a) Type i1, b) Type i2, c) Type ii1, d) Type ii2, e) Type ii3, f) Type iii1, g) Type iii2, and h) Type iv specimens.

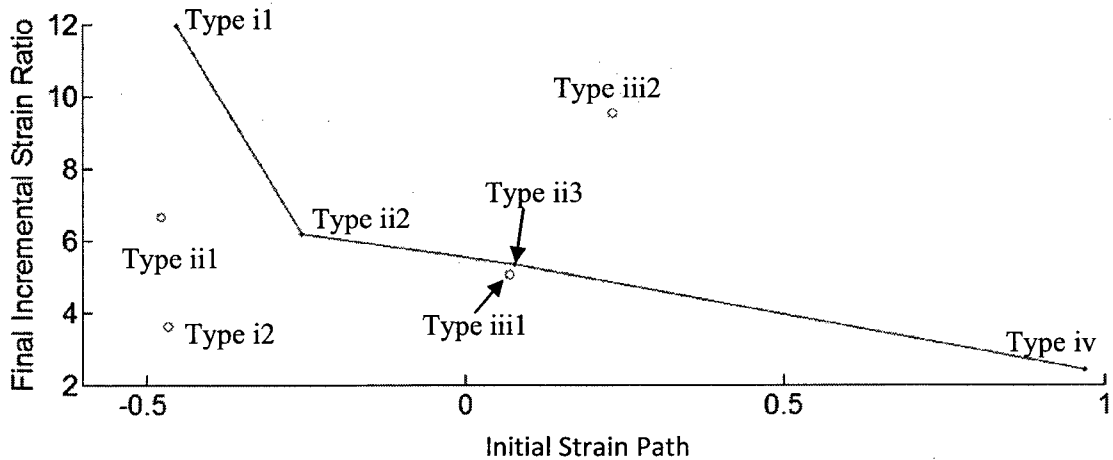


Figure 3-8: Initial strain path versus incremental strain ratio for image directly before failure.

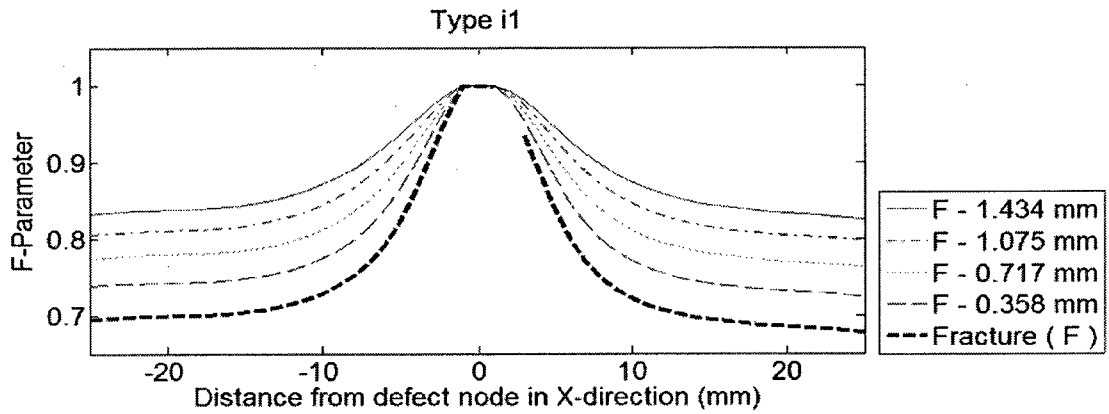
3.2 Results for Derov et al. Model Key Assumption

Similar to the M-K model, the Derov et al. model includes a key assumption with respect to a critical stress concentration factor (i.e., F-parameter) at failure, which is a ratio of the effective stress in the safe region to the effective stress in the defect region. Since the stress values at the defect location are always expected to be higher than the other areas, the F-parameter is always less than unity.

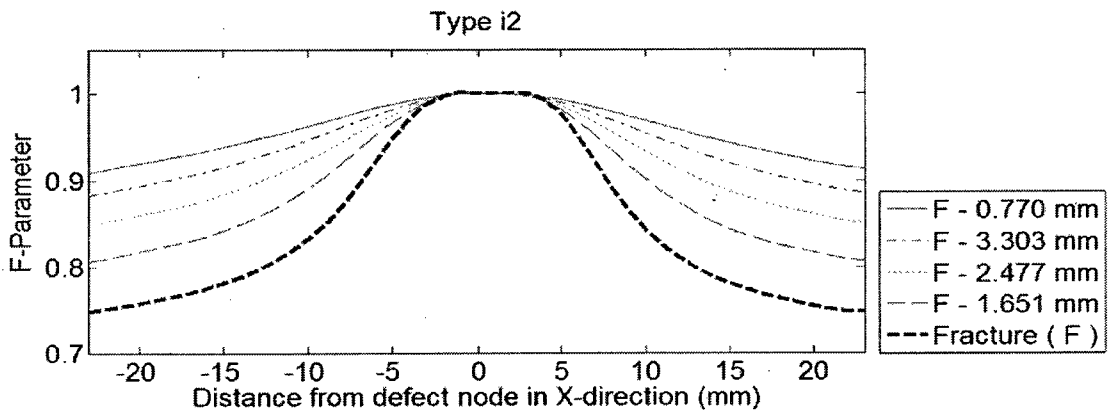
Data was analyzed at four different images before failure (i.e., 0.75-3 seconds before failure for Type i1 and i2 specimens and 1-4 seconds for the other specimens). The reason for choosing different time amounts was to capture the failure and strain effects between the subsequent images (i.e., approximately 1% strain difference between images). To be consistent with the M-K analysis, the highest major strain location was selected as the defect node (see the derivation in Appendix A). For most specimens, the defect node had the F-parameter of unity. Figure 3-9 shows plots of X-direction location versus F-parameter. The five curves are labelled with respect to the

punch location prior to failure (i.e., in Fig. 3-9a), the punch would travel 0.3585 mm between digital images). The punch distances were measured using the LRT attached to the central punch cylinder. As shown in Fig. 3-3, the X-direction location is the perpendicular distance from defect node.

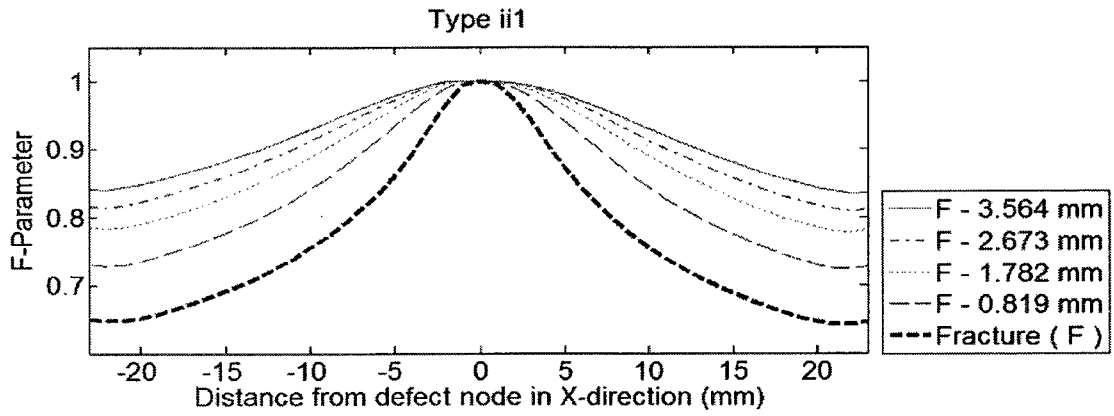
a)



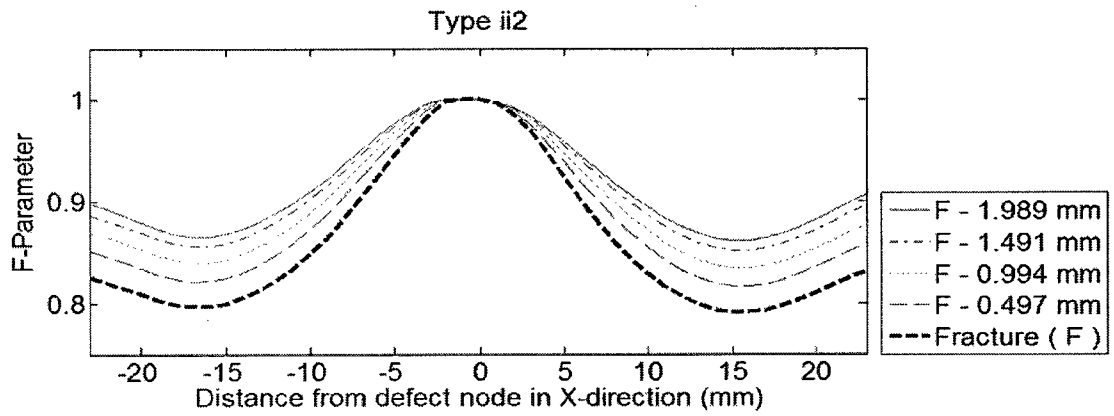
b)



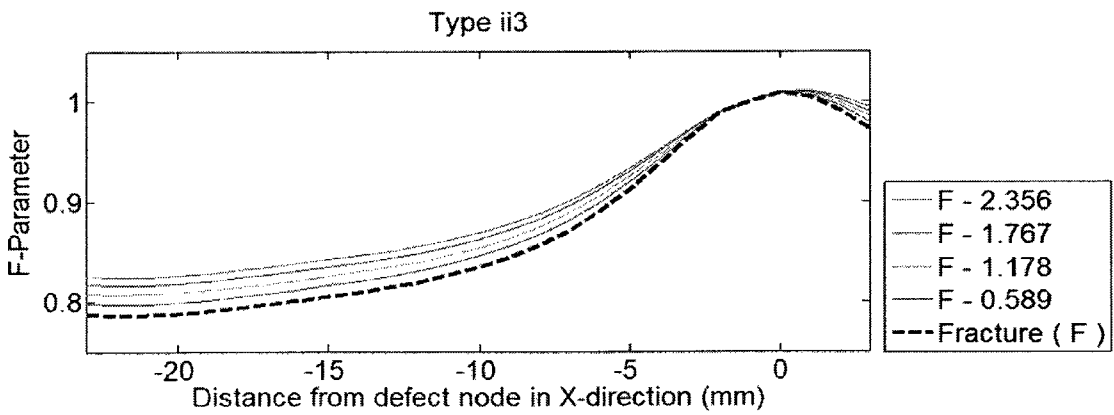
c)



d)



e)



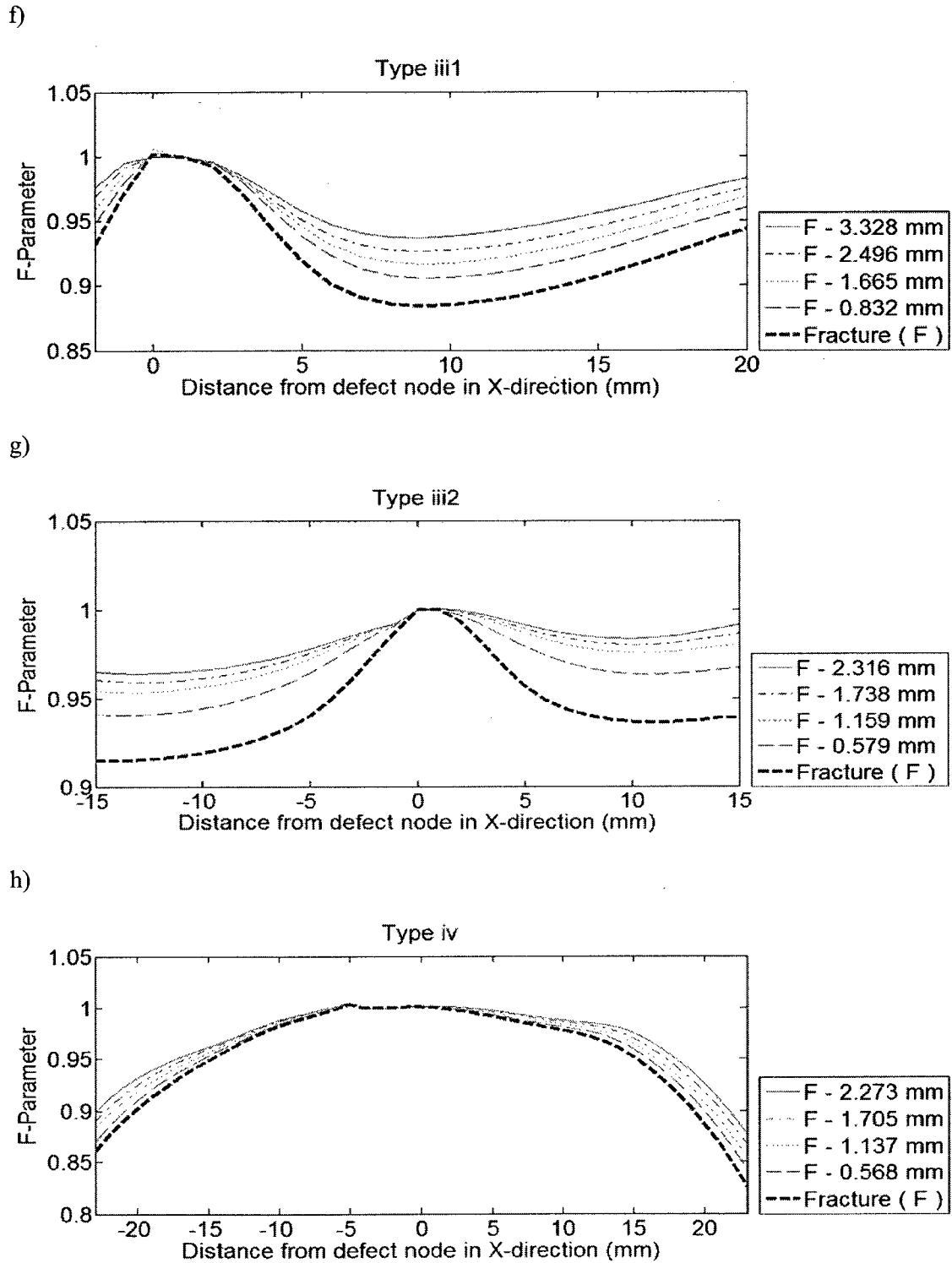


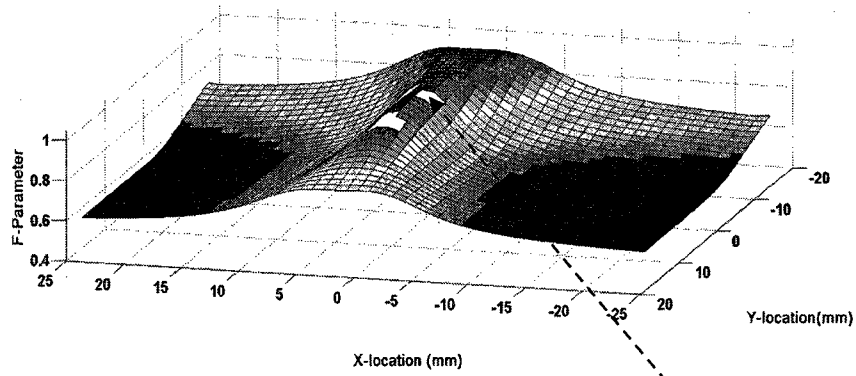
Figure 3-9: Critical stress concentration factor (i.e., F-parameter) versus the X-direction location for a) Type i1, b) Type i2, c) Type ii1, d) Type ii2, e) Typeiii3, f) Type iii1, g) Type iii2 and h) Type iv specimens.

In Fig. 3-9 a), for the uniaxial case, the F-parameter becomes relatively constant after a distance of 10 mm away from the defect location. This could represent the safe region of the specimen. For other specimen geometries, the F-parameter continues to linearly decrease beyond 10 mm; thus, the “safe” region is not as easily defined. Note that for Fig. 3-9 h) (i.e., the balanced biaxial geometry), the F-parameter is approximately unity for -10 to 10 mm in the X-direction from the defect. This is due to the large defect area as observed in Fig. 3-3h). Also, in Fig. 3-9 d), for the Type ii2 specimen, the F-parameter increases after 15 mm away from the defect. In the paper by Wilson et al. [14], this effect was also observed for a balanced biaxial specimen with a single defect location.

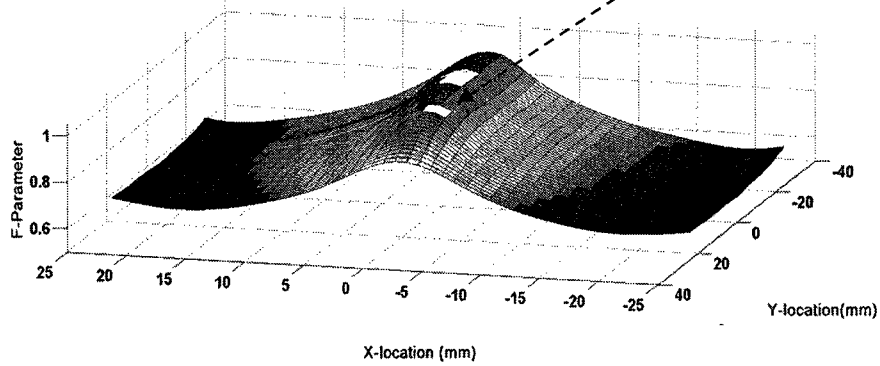
For Figs. 3-9 f) and g), the F-parameter is shown for a wider location on one side of the specimen since the failure was near to the radius of the punch. For Fig. 3-9 f), the F-parameter decreased to a certain point and started increasing due to another concentrated defect region. This effect was also seen in the contour plots (See Fig. 3-3 f)).

Figure 3-10 shows the spatial distribution of F-parameter right before failure versus both X- and Y- distances from the defect node for only three geometries as trends are consistent. Note that the spatial variation along the defect direction (i.e., Y-direction) is consistent for these specimens. In Fig. 3-10 a) and b), as in the 2D plots of Fig. 3-9 for these geometries, the locations of high critical stress concentrations are well defined. However, for the Type iv case in Fig. 3-10c), the near unity F-parameter spatial distribution has a relatively large width as observed in Fig. 3-9f).

a)



b)



c)

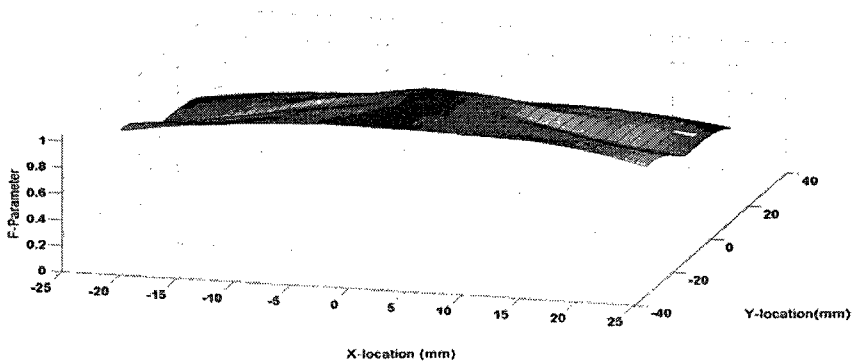


Figure 3-10: Surface plot of critical stress concentration factor (i.e., F-parameter) versus location from defect node for a) Type i2, b) Type ii1 and c) Type iv specimens.

F-parameter values were also compared with respect to different specimen geometries with strain paths varying from uniaxial to balanced biaxial. Figure 3-11 shows that as the initial strain path increases (e.g., Type i1 for uniaxial and Type iv for balanced biaxial), the width of the defect region increases. This effect is also physically reasonable. As the width area of the specimen increases, the defect region for the specimen increases as shown in the strain contour plots of Fig. 3-3. Note that Type ii2 and ii3 specimens have approximately the same defect width size.

Figure 3-12 shows the F-parameter values with respect to the initial strain path in the “safe” region at both 5 and 10 mm away from the defect location. As the initial strain path increases in the specimen, the F-parameter value increases.

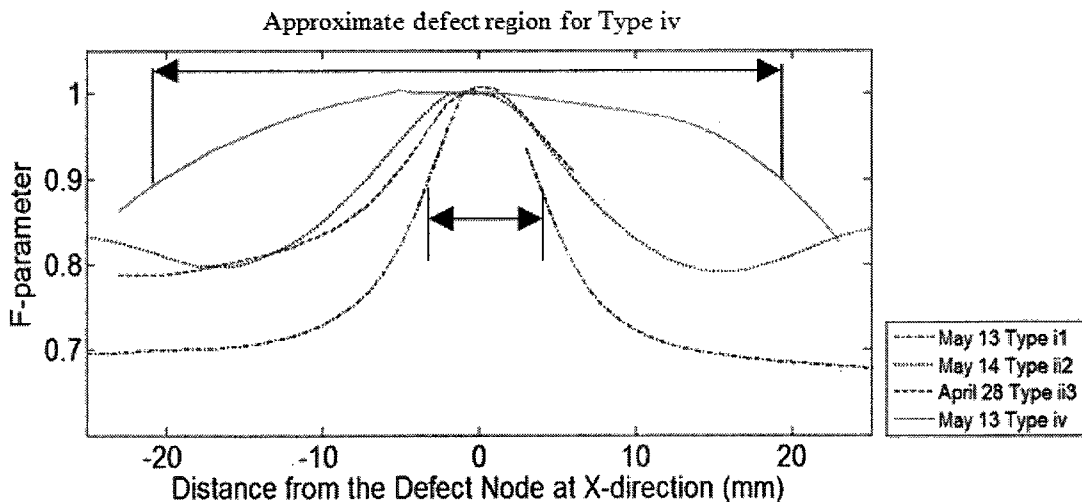


Figure 3-11: Critical stress concentration factor (i.e., F-parameter) versus distance from the defect node in the X-direction for different specimen types. (F-parameter for Type ii3 is centered to see the effect)

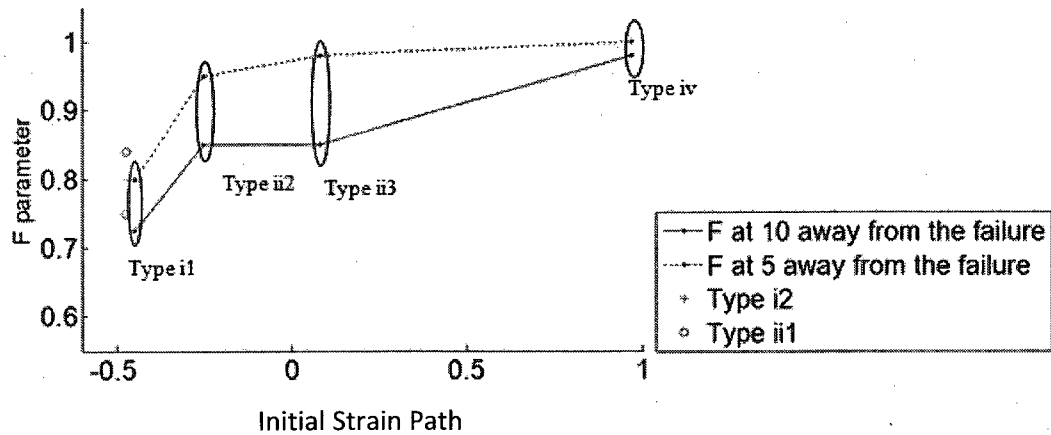


Figure 3-12: Critical stress concentration factor (i.e., F-parameter) versus initial strain path. (Note that curves represent data 5 and 10 mm away from the defect locations.)

3.3. Discussions

The experimental results show that the key assumptions in both the M-K and Derov et al. models are not completely supported by the experimental data. The incremental strain ratio to indicate failure for the M-K model is expected to be a constant value for every strain path. However, as shown in Fig. 3-9, the incremental strain ratio decreases with increasing initial strain path values. Note however the nearly vertical slope of the curves in Fig. 3-7 just prior to failure. Thus while the incremental strain ratio values were not a constant value (e.g., $\frac{\Delta\varepsilon_{1B}}{\Delta\varepsilon_{1A}} = 10$), only a small amount of further deformation would have been necessary to achieve this value.

Note that another key assumption in the M-K model is the initial thickness ratio between the safe and defect regions. For the experiments conducted, such a thickness defect did not exist. Furthermore, there was nothing in the experimental results which could be used to investigate this assumption. The critical stress concentration factor in

the Derov et al. model is analogous to both the incremental strain ratio and the thickness ratio assumptions in the M-K model.

For the key assumption in the model by Derov et al., the critical stress concentration factor was not constant at a given X-direction location for the various initial strain paths either (see Fig. 3-12). This is due to the saturation (i.e., levelling off) of the stress-strain relationship at high strain values. Despite the higher strain values in the defect region as shown in Figs. 3-3 and 3-5, the calculated critical stress concentration factor did not decrease significantly. Furthermore, the width of the defect region increased as the strain path varied from a uniaxial to balanced biaxial case. For the Type iv case, the F-parameter was near unity over a 20-30 mm range. This is much larger than a thin deformation zone assumed in both the M-K and Derov et al. models (see Fig. 3-11).

For neither the M-K or Derov et al. models did a constant parameter to predict failure exist. The M-K model though had a more consistent location of the safe region (approximately 5 mm away from the defect node) and reasonable size of the defect region compared to the Derov et al. model which had a defect size of approximately 20-30 mm for the balanced biaxial case. Conversely, the defect locations as shown in the strain contour plots are approximately the same size as the regions with high critical stress concentration factors in Figs. 3-9 and 3-11.

Note that for these comparisons of both the M-K and Derov et al. model assumptions, data was obtained to represent failure at the image directly before a physical tearing failure was observed. However, plastic instability would have occurred prior to this

image. This particularly would have affected the results from the M-K analysis as the deviation of the strain path in the defect region is supposed to signify plastic instability. Note that this would decrease the incremental strain ratio at failure and a typical value to predict failure is already lower than expected (i.e., $\frac{\Delta\varepsilon_{1B}}{\Delta\varepsilon_{1A}} = 10$) for all geometries except the uniaxial case.

Data from Type i2, iii1 and iii2 specimens did not follow the same trends as the other specimen data for both the M-K and Derov et al. models. Types iii1 and iii2 geometries provided reasonable strain paths. However, Type iii1 specimens failed at low strain values (see Fig. 3-1), and for Type iii2 specimens, the incremental strain ratio at failure was higher than the trend (see Fig. 3-8). Similarly, for the Type i2 specimen, a well defined defect region was obtained (see Fig. 3-3); however, the incremental strain ratio for the specimen geometry is unreasonably low and the width of the defect region is wider than Type i1 specimens due to the increased width of the specimen. The other specimen which was not used in the line graphs throughout this chapter is specimen Type ii1. While the trends are reasonable with respect to the other Type ii specimens, the strain path was nearly redundant with Type i1. These results show that while the desired strain paths are created with the Raghavan modification to the Marciniak tests, the key model assumption parameters obtained do not follow trends. Therefore, further modifications to these specimen geometries may be necessary.

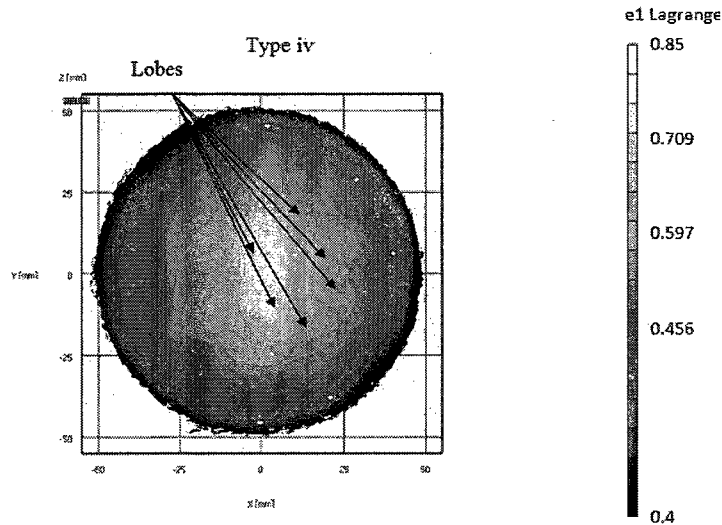


Figure 3-13: Contour plot of major strain for balanced biaxial case (specimen Type iv).

Similar investigations to these were conducted on Al 6022-T4 [14] but for only plane strain and balanced biaxial cases. The balanced biaxial specimens for Al 6022-T4 displayed both multiple and single defects; however, for the balanced biaxial cases in the experiments conducted here on 1018 steel, one large defect with “lobes” occurred for both of the trials (see Fig. 3-13 for the strain contour plot of another balanced biaxial case). Also, strain paths in Wilson et al. [14] showed minimum divergence for the strain path 15mm away perpendicular to the defect location for the Al-6022 biaxial case. Conversely, for the 1018 specimens, an early divergence at 10 mm perpendicular to the defect region was observed. Finally, Wilson et al. found that the incremental strain ratio for aluminium was approximately 1.6 for the balanced biaxial cases. However, for the steel specimens, the incremental strain ratio was higher for the balanced biaxial case (i.e., 2.5). All of these results can be explained by the different material (Al 6022-T4 and 1018 steel) used in these studies. For steel, after plastic instability, the material deforms more prior to failure. This causes an increase in the localization of the failure and higher strain values and corresponding stress

values. For the plane strain cases, Wilson et al. only analyzed the strain paths and the F-parameter values. Similar results to those in Fig. 3-5e) and Fig. 3-9e) for 1018 steel were observed respectively.

CHAPTER 4

CONCLUSIONS

In this research, the key assumptions in the M-K and Derov et al. failure models were investigated by conducting Marciniak tests on 1018 steel to determine the related parameters of interest. Strain was measured in the process using Digital Imaging Correlation (DIC) and was converted to a critical stress concentration factor (i.e., F-parameter) assuming Hill's 1948 yield criterion, force equilibrium perpendicular to the defect region, and conservation of volume. Strain paths generated from the Marciniak tests produced a reasonable distribution between uniaxial and balanced biaxial cases.

For the M-K model, while a concentration of major strain existed in the defect region compared to the safe region, the incremental strain ratio at failure was not constant but decreased as the initial strain path for the specimen increased. However, the trajectory of the incremental strain ratio curves was such that a plane strain state existed in the defect region at failure. The safe region was shown to be approximately 5 mm away from the defect region for all specimen geometries. Note that the typical means to conceptualize failure in the M-K model (i.e., the defect region strain path diverging from the safe region strain path) does not occur for specimen geometries with uniaxial and plane strain paths.

For the Derov et al. model, the F-parameter was also not constant for the various initial strain paths. Also, the size of the defect varied, which is expected due to the varying specimen geometries. Despite the higher strain values in the defect region as observed with the DIC system, the saturation of effective stress for the stress-strain relationship caused the F-parameter for the balanced biaxial case to not decrease significantly when considering locations perpendicular to the defect region. But the F-parameter was able to characterize the localization of deformation, the size of the defect region, and distinction between the safe and the defect regions. The results in this research were consistent with the past work by Wilson et al. [14] for Al 6022-T4 except that “lobed” defect areas existed for the balanced biaxial strain path cases, which is likely due to the material tested.

While reasonable strain paths were produced from the experiments, some of the specimen geometries did not follow the trends observed for the key assumption parameters. These results are due to the specimen and sacrificial washer geometries used. In addition, some specimen geometries produce redundant strain paths. Thus, further research is needed to improve the Marciniak tests so consistent deformation not just with respect to strain paths is achieved and more distinct strain paths are generated.

CHAPTER 5

FUTURE WORK

The results of the experimental work presented in Chapter 3 raise the questions about key assumptions in the analytically predicted stress and strain-based FLDs. In particular, the Derov et al. model is being further developed to capture the effects of defect orientations. Furthermore, Finite Element (FE) Simulations of the Marciniak Test are conducted. These simulations are for both M-K model and Derov et al. model should be compared with experimental results. For this thesis, only steel specimens are tested for different geometries. Aluminium specimens should also be tested for all strain paths in order to comment on the M-K and Derov et al. models compatibility for different materials. The specimen types giving redundant strain paths should be replaced with ones that provide different positive minor strain values.

In addition the biaxial testing machine for testing the specimens without any geometry modification should be ready shortly. This will allow testing the specimens under different principal stresses without using different geometries.

LIST OF REFERENCES

- [1] Keeler, S. P., 1966, "Determination of Forming Limits in Automotive Stampings", Transactions of Society of Automotive Engineers, Paper No. 650355.
- [2] Graf, A. and W. Hosford (1993), "Effect of Changing Strain Paths of Forming Limit Diagrams of AL 2008-T4", Metallurgical Transactions, Vol. 24A, pp. 2503-12.
- [3] Graf, A. and W. Hosford (1990), "Calculations of Forming Limit Diagrams", Metallurgical Transactions A, Vol. 21A, pp. 87-94.
- [4] Matthew J. Derov, Igor Tsukrov, and Brad L. Kinsey (2009) "Analytical Prediction of Shifting Behavior in Strain Based Forming Limit Curves for Sheet Metal Using a Stress Based Failure Criterion", Transactions of the North American Manufacturing Research Institute of SME, Vol. 37, pp. 293-300.
- [5] D. Zeng, L. Chappuis, Z. Cedric Xia, and Xinhai Zhu (2008) "A Path Independent Forming Limit Criterion for Sheet Metal Forming Simulations", SAE Paper 2008-01-1445.
- [6] Stoughton, T.B. (2001), "Stress-Based Forming Limits in Sheet-Metal Forming", Journal of Engineering Materials and Technology, Vol. 123, Oct., pp.417-422.
- [7] Marciniak, Z. and K. Kuczynski (1967) "Limit Strains in the Process of Stretch-Forming Sheet Metal", International Journal of Mechanical Sciences, Vol. 9, pp. 609-20.
- [8] Yao, Hong and Cao, Jain (2002) "Prediction of Forming Limit Curves Using and Anisotropic Yield Function with Prestrain Induced Backstress", International Journal of Plasticity, Vol. 18, pp. 1013-1038
- [9] Derov M., Kinsey B., Tsukrov I. (2008) "The effect of model parameters on predicted stress based failure criterion for sheet metal", Proceedings of MSEC 2008
- [10] K.S. Raghavan: Metall. Mater. Trans. A, 1995, vol. 26A, pp. 2075-84.

[11] Hassan R, 2009, Unpublished Work

[12] Correlated Solutions Inc., Vic-3D 2007 Testing Guide, CSI Application Note AN-525. "Speckle Pattern Fundamentals".

[13] R. Hill, Proc. Roy. Soc. London, 193A (1948), p. 281 and Mathematical Theory of Plasticity, Chapter. XII (London: Oxford University Press, 1950).

APPENDICES

APPENDIX A

MARCINIAK-KUCZYNSKI MODEL DESCRIPTION

Marciniak and Kuczynski pointed out that for the localized necking to occur in biaxial stretching, the strain state should be changing to a plane strain condition. For sheet metal forming, the material is anisotropic, which is represented by the ratio of the width strain to the thickness strain, i.e., R parameter. It is assumed that a plane stress condition exists ($\sigma_3 = 0$). The yield criterion can be described as following:

$$|\sigma_1|^a + |\sigma_2|^{a+R}|\sigma_1 - \sigma_2|^a = (R + 1)\overline{\sigma}^a \quad (\text{B.1})$$

The values for the higher order criterion are suggested as $a=6$ for bcc metals (e.g., steel) or $a=8$ for fcc metals (e.g., Aluminium); however, for Hill's 1948 criterion, this value is assumed to be 2.

For the M-K analysis, for the right side of the strain-based FLC (i.e., positive minor strains), it is assumed that there is an initial imperfection in the form of a long groove oriented 90 degrees to the direction of major principal stress. The initial imperfection is characterized by the thickness ratio:

$$f = \frac{t_{b0}}{t_{a0}} \quad (\text{B.2})$$

In addition, it is assumed that the strains parallel to the groove are equal in both regions:

$$\varepsilon_{2a} = \varepsilon_{2b} \quad (\text{B.3})$$

The stress ratio outside the groove is constant during the whole process:

$$\sigma_2 = \frac{\sigma_{2a}}{\sigma_{1a}} \quad (\text{B.4})$$

At all times during the process the force balance across the groove must be satisfied:

$$\frac{\sigma_{1a}}{\sigma_{1b}} = f \exp(\varepsilon_{3b} - \varepsilon_{3a}) \quad (\text{B.5})$$

A strain increment $\Delta\varepsilon_{1b}$ is imposed in the groove and the corresponding values of $\Delta\varepsilon_{1a}$ and $\Delta\varepsilon_{2a}$ are calculated. This procedure is repeated with new strain increments (i.e., $\Delta\varepsilon_{1b}$) until the strain increment $\Delta\varepsilon_{1a}$ is very small in comparison (e.g., the ratio is greater than 10).

The step by step instruction for applying the M-K model for a FLC is stated:

1. Specify $\Delta\varepsilon_{1b}$ and $\rho_a = \frac{\Delta\varepsilon_{2a}}{\Delta\varepsilon_{1a}}$.
2. Guess initial $\Delta\varepsilon_{1a}$
3. Using ρ_a calculate $\alpha_a = \frac{(1+\frac{1}{R})\rho_a+1}{\rho_a+(1+\frac{1}{R})}$
4. From ρ_a calculate $\Delta\varepsilon_{2a} = \rho_a \Delta\varepsilon_{1a}$
5. From ρ_a calculate $\Delta\bar{\varepsilon}_a = \frac{R+1}{\sqrt{2R+1}} \Delta\varepsilon_{1a} \sqrt{1 + \rho_a^2 + \frac{2R}{R+1} \rho_a}$
6. Assume $\Delta\varepsilon_{2a} = \Delta\varepsilon_{2b}$
7. From $\Delta\varepsilon_{2b}$ and $\Delta\varepsilon_{1b}$ calculate $\rho_b = \frac{\Delta\varepsilon_{2b}}{\Delta\varepsilon_{1b}}$
8. From ρ_b calculate $\alpha_b = \frac{(1+\frac{1}{R})\rho_b+1}{\rho_b+(1+\frac{1}{R})}$
9. From ρ_b calculate $\Delta\bar{\varepsilon}_b$ analogous to step 5.
10. If this is not the initial step from zero strain state, add the increment values calculated to $\bar{\varepsilon}_a$ and $\bar{\varepsilon}_b$.
11. From $\Delta\bar{\varepsilon}_b$ and $\bar{\varepsilon}_b$ calculate $\bar{\sigma}_b = K(\bar{\varepsilon}_b + \Delta\bar{\varepsilon}_b)^n$
12. Calculate total ρ_b from $\rho_b = \frac{\varepsilon_{2b} + \Delta\varepsilon_{2b}}{\varepsilon_{1b} + \Delta\varepsilon_{1b}}$
13. Also calculate total α_b analogous to step 8.

14. From α_b calculate $\phi_B = \sqrt{\frac{\alpha^2 + 1 + (1 - \alpha)^2}{1 + R}}$

15. From α_b calculate $\sigma_{1b} = \frac{\bar{\sigma}_B}{\phi_B}$

16. Repeat the steps 13-15 for region a.

17. Calculate the thickness strains $\Delta\varepsilon_{3b} = -\Delta\varepsilon_{1b} - \Delta\varepsilon_{2b}$

18. And analogously $\Delta\varepsilon_{3a} = -\Delta\varepsilon_{1a} - \Delta\varepsilon_{2a}$

19. Calculate a $\Delta\bar{\varepsilon}_a$ from values calculated using

$$\Delta\bar{\varepsilon}_{a\text{calc}} = [f \exp^{(\varepsilon_{3b} + \Delta\varepsilon_{3b}) - (\varepsilon_{3a} + \Delta\varepsilon_{3a})} \left(\frac{\phi_A}{\phi_B}\right) (\bar{\varepsilon}_b + \Delta\bar{\varepsilon}_b)^n]^{1/n} - \bar{\varepsilon}_a$$

20. Calculate ρ_a analogous to step 5.

21. Calculate $\Delta\varepsilon_{1\text{calc}} = \frac{\Delta\bar{\varepsilon}_{a\text{calc}}}{\frac{R+1}{\sqrt{2R+1}} \sqrt{1 + \rho_a^2 + \frac{2R}{R+1} \rho_a}}$

22. Define an error $Error = \Delta\varepsilon_{1\text{guess}} - \Delta\varepsilon_{1\text{calc}}$

23. If $Error < \text{threshold break}$, otherwise iterate to step 2 until Error becomes small.

This generates the strain path in the safe and defect regions. Failure is predicted to occur once a plane strain condition in the defect region exists. The strain state in the safe region is plotted as a point on the forming limit curve. Then this procedure is repeated for various strain paths in step 1 to determine the strain-based FLC

APPENDIX B

Derov et al. Model Description

Similar to M-K model, the failure criterion proposed by Derov et al. suggests a stress concentration factor (i.e., F-parameter) to determine the material failure. Since Derov et al. model is a stress-based failure criterion, a F-parameter should be specified and a major stress component should be determined as an initial guess. Afterwards, the stresses and strains inside and outside the defect region can be determined. The calculation starts with the effective stress computation:

$$\begin{aligned}\overline{\sigma}_A &= \sqrt{\sigma_{1A}^2 + \sigma_{2A}^2 - \sigma_{1A}\sigma_{2A}} \\ \overline{\sigma}_A &= \sqrt{\sigma_{1A}^2 + \frac{1+r_{90}}{r_{90}} \frac{r_0}{1+r_0} \sigma_{2A}^2 - \frac{2r_0}{1+r_0} \sigma_{1A}\sigma_{2A}}\end{aligned}\tag{B-1}$$

The inputs of the model are a yield criterion and a constitutive relationship. In Eq. B-1, the effective stress is calculated using Von Mises and Hill's 1948 yield criteria respectively. For Hill's criterion, the anisotropic parameters r_0 and r_{90} are used. Then the stress ratio (α) is defined as:

$$\alpha_A = \frac{\sigma_{2A}}{\sigma_{1A}}\tag{B-2}$$

There is an explicit relationship between the strain and the strain ratio which can be defined with Eq. B-3 for Von Mises and Hill's 1948 yield criteria respectively:

$$\rho_A = \frac{2\alpha_A - 1}{2 - \alpha_A} \quad (\text{B-3})$$

$$\rho_A = \frac{\alpha_A \left(1 + \frac{1}{r_{90}} \right) - 1}{1 + \frac{1}{r_0} - \alpha_A}$$

The effective strain values are calculated using the power hardening law. Note that K is the strength coefficient and n is the strain hardening coefficient:

$$\bar{\varepsilon}_A = \left(\frac{\bar{\sigma}_A}{K} \right)^{1/n} \quad (\text{B-4})$$

From the effective strain, the principle strains in major and minor directions can be found using the work-energy principle:

$$\varepsilon_{1A} = \frac{\bar{\sigma}_A \cdot \bar{\varepsilon}_A}{\sigma_{1A} (1 + \alpha_A \rho_A)} \quad (\text{B-5})$$

$$\varepsilon_{2A} = \frac{\bar{\sigma}_A \cdot \bar{\varepsilon}_A - \sigma_{1A} \cdot \varepsilon_{1A}}{\sigma_{2A}} \quad (\text{B-6})$$

All stress and stress components for the safe region are now computed, but the values in the defect region must be found. In order to relate the safe and the defect regions, the F-parameter is used to relate the effective stresses:

$$\overline{\sigma}_A = F \cdot \overline{\sigma}_B \quad (\text{B-7})$$

Using the power hardening law, the equivalent strain in the defect region can be obtained from:

$$\overline{\varepsilon}_B = \sqrt[n]{\frac{\overline{\sigma}_B}{K}} \quad (\text{B-8})$$

The strain equality inside and outside the defect region in the 2-direction is also an assumption for the Derov et al. model. Since the equivalent strain is calculated from Eq. B-8, the major strain in the defect region can be calculated using:

$$\overline{\varepsilon}_B = \sqrt{\frac{4}{3}(\varepsilon_{1B}^2 + \varepsilon_{2B}^2 + \varepsilon_{1B}\varepsilon_{2B})} \quad (\text{B-9})$$

$$\overline{\varepsilon}_B = \sqrt{\frac{(1+r_0)(1+r_{90})}{1+r_0+r_{90}}} \sqrt{\varepsilon_{1B}^2 + \frac{1+r_0}{r_0} \frac{r_{90}}{1+r_{90}} \varepsilon_{2B}^2 + \frac{2r_{90}}{1+r_{90}} \varepsilon_{1B}\varepsilon_{2B}}$$

for Von Mises and Hill's yield criteria respectively.

Equations (B-5) and (B-6) can then be used inside the defect to obtain σ_{1B} and σ_{2B} . The condition to verify whether the guessed value of σ_{1A} is a reasonable value is the force equilibrium in the 1-direction. Using Eq. B-11, the calculated value σ_{1A}^o is computed:

$$\sigma_{1A}^o = \sigma_{1B} \exp(\varepsilon_{3B} - \varepsilon_{3A}) \quad (\text{B-11})$$

If the guessed and the calculated major stress in the safe region has a large discrepancy, the guessed value of major stress is incremented and the calculations are repeated for a new value. When the values are within a small error, the values satisfy the failure condition. The calculations of the failure parameters are repeated for various values of minor strain in the safe region, to construct a complete stress-based Forming Limit Curve (FLC).

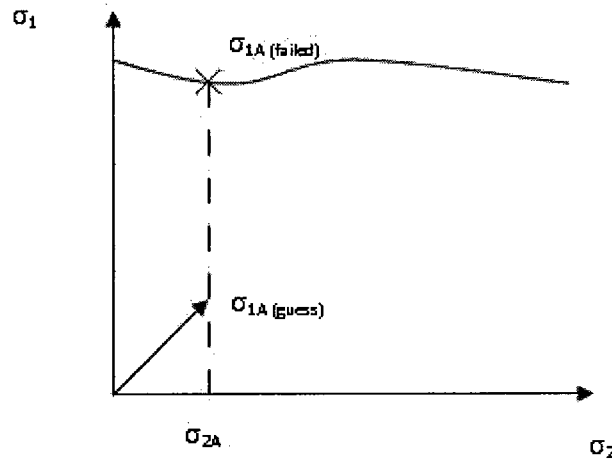


Figure B-1: Incremental path showing how to calculate the stress-based FLC. Once one set of failure points is found, the σ_{2A} is incremented and another set is calculated.